Article

Contribution of Triassic Tectonomagmatic Activity to the Mineralization of Liziyuan Orogenic Gold Deposits, West Qinling Orogenic Belt, China

Shuo Wang [1,2], Zhanjin Liu [1], Yunhua Liu [1,*], Nan Deng [3], Benzhao Yang [4] and Le Tan [4]

[1] School of Earth Sciences and Resource, Chang'an University, Xi'an 710054, China
[2] Key Laboratory of Mineral Resources Evaluation in Northeast Asia, Ministry of Natural Resources, Changchun 130061, China
[3] Xi'an Mineral Resources Survey Center, China Geological Survey, Xi'an 710100, China
[4] Geological Team No. 1 of Shaanxi Bureau of Geology and Mineral Resources, Ankang 725000, China
[*] Correspondence: zyyhliu@chd.edu.cn

Abstract: The Western Qinling orogenic belt (WQOB) is one of the most important prospective gold districts in China, with widely distributed Indosinian intermediate–acidic intrusions. The Liziyuan Au deposit is a representative orogenic deposit in the northern WQOB, hosting several sections spatially associated with igneous rocks. The Au deposit is hosted by meta-sedimentary volcanic rocks of the Cambrian–Ordovician Liziyuan Group and the Tianzishan monzogranite. Two periods, including five stages of mineralization, are recognized in this area: an early metamorphic mineralization period (PI), including quartz–pyrite (Stage I) and banded quartz–polymetallic sulfide (Stage II) veins, and a later magmatic mineralization period (PII) including quartz–K-feldspar–pyrite–molybdenite veins (Stage III), quartz–polymetallic sulfide–chlorite ± calcite veinlets and stockwork (Stage IV), and late calcite–quartz veinlets (Stage V). Geochronological studies indicate a SHRIMP zircon U-Pb age of 236.1 Ma for the Tianzishan monzogranite, and our published ages of ore-bearing diorite porphyrite of the Suishizi section and granite porphyry of the Jiancaowan section being 213 and 212 Ma, respectively. Pyrites formed in association with PI and PII mineralization have well-defined Rb–Sr ages of 220 ± 7.5, 205.8 ± 8.7, and 199 ± 15 Ma, with close temporospatial coupling between mineralization and magmatism. The $\delta^{18}O$ and δD values of fluid inclusions in Stage IV auriferous quartz veins range from −0.03‰ to +5.24‰ and −93‰ to −75‰, respectively, suggesting that mineralizing fluid was likely of magmatic origin. Three distinct ranges of $\delta^{34}S$ values are identified in the studied sections (i.e., 7.04‰–9.12‰, −4.95‰ to −2.44‰, and 0.10‰–3.08‰), indicating a source containing multiple sulfur isotopes derived from magmatic and metamorphic fluids. The Liziyuan Au deposit is thus likely an orogenic deposit closely related to magmatism. Geochemical characteristics indicate that Tianzishan monzogranite is adakitic and was derived from thickened lower crust during Triassic orogenesis. The ore-bearing diorite porphyrite and granite porphyry formed in a post-collision extensional setting. Together with previous geological and geochemical data, our results indicate that the Liziyuan orogenic Au deposit was formed by early collisional–compressional metamorphism and late post-collision extensional magmatic fluids related to the evolution of the WQOB.

Keywords: Western Qinling orogenic belt; Liziyuan orogenic Au deposit; geochronology; S–H–O isotopes; tectonomagmatism; adakite; mineralization

1. Introduction

Orogenic gold deposits have attracted increasing research attention over recent decades [1–6], with their large proportion of global Au reserves typically being developed in metamorphic terranes and structurally controlled by compressional to transpressional structures associated with accretionary and/or collisional orogenic tectonic

settings [6–10]. Country rocks related to orogenic Au deposits include granitic intrusions [3,11] and metasedimentary and metabasaltic rocks [12–16]. However, the correlation between orogenic Au deposits and tectonomagmatic activities remains controversial [7,17] because it is difficult to identify Au fluid sources containing metamorphic fluids derived from the dewatering of supracrustal rocks [9,18], lower crust/mantle fluids [6,10,19–21], or orogenesis-related granitic magmatic solutions [22,23], especially where there are clear temporospatial relationships between deposits and intrusions. Although most of the published signatures of ore-forming fluids are consistent with those of metamorphic source fluids, a magmatic–hydrothermal genesis has recently come back into favor [24–26].

With the discovery of several large Au deposits, such as the Anba, Zaozigou, Yangshan, Liba, Jinlongshan, and Zhaishang deposits, the West Qinling orogenic belt (WQOB) has become one of the most important prospective gold provinces in China, containing over 2000 tonnes of Au in what are generally classified as Carlin, Carlin-like, and orogenic-type deposits [27–31]). However, debate remains on whether magmatism contributed to the mineralization of orogenic gold deposits in the WQOB, which contains numerous Triassic intrusions hosted in or coexisting with orebodies that represent intrusion-related or orogenic mineral systems. The Liziyuan Au deposit is a typical example hosted in brittle to ductile shear zones developed in greenschist-facies metasedimentary volcanic rocks and Triassic intrusions, making it an ideal site for investigation of the relationship between orogenic mineralization and magmatism. In this study, we undertook whole-rock geochemical analysis of Triassic intrusions related to the deposit, S–H–O isotope geochronological analyses, and detailed deposit-scale geological characterization with the aim of constraining the magmatism and mineralization of the Liziyuan Au deposit. Our results may provide new insights into the role of magmatism during the formation of such orogenic deposits.

2. Geological Setting

The Qinling orogenic belt is in central China (Figure 1a) and includes three blocks and two sutures [32,33], connecting to the Kunlun–Qilian Orogen in the west and the Sulu–Dabie Orogen in the east, formed during multiple Paleozoic–Mesozoic subduction–collision–accretion events between the North China and Yangtze cratons [34–37]. The WQOB is tectonically separated from the Qilian Orogen and North Qinling Block by the Lin(xia)–Wu(shan)–Tian(shui) fault and the Shangdan suture to the north (Figure 1b) and the Animaqing–Mianlue suture to the south, and it is traditionally separated from the East Qinling orogenic belt by the Huicheng Basin or the Foping Uplift along the Bao(ji)–Cheng(du) railway.

Paleozoic–Mesozoic strata are widespread in the WQOB. Proterozoic metamorphic volcanic–sedimentary formations (846–776 Ma) occur in the southeast [38,39], and Devonian–Triassic sedimentary rocks are widely exposed. These strata have been strongly folded and faulted during Triassic accretion and collision [40,41]. Paleozoic strata are the main host rocks of the Au deposit [42–44]. Early Mesozoic granitoid intrusions are widely exposed in the WQOB and are recognized as having been generated during the evolution of the Paleo-Tethys Ocean between the North and South China blocks [45–47].

The Liziyuan Au deposit lies in the northern WQOB and has been a major target for Au–polymetallic exploration in recent decades. Exposed strata in the mining area include the middle–lower Proterozoic Qinling Group comprising high-grade metamorphic rocks (Figure 1c); the Cambrian–Ordovicinan Liziyuan Group comprising a fore-arc volcanic–sedimentary complex; the Upper Ordovician Caotangou Group, which is characterized by the occurrence of volcanoclastic rocks and lava; the Middle Devonian Shujiaba Formation comprising metamorphosed siltstone, sandstone, mudstone, and shale; the Upper Devonian Dacaotan Group comprising sandstone and conglomerate, which formed in fluvial and lacustrine settings [48], and Cenozoic cover. Triassic intrusions are widespread, as represented by the Tianzishan, Baguashan, and Chaijiazhuang plutons, and later widespread intermediate–acid dikes are spatially associated with Au orebodies. The NW-trending

ore-hosting shear zones run parallel to the regional integral structure and are intersected by later NE-trending brittle faults. Orebodies in the Liziyuan Au deposit are hosted by brittle to ductile shear zones in greenschist-facies metasedimentary volcanic rocks and the Tianzishan monzogranite, and the deposit contains three main sections at Shenjiagou, Suishizi, and Jiancaowan.
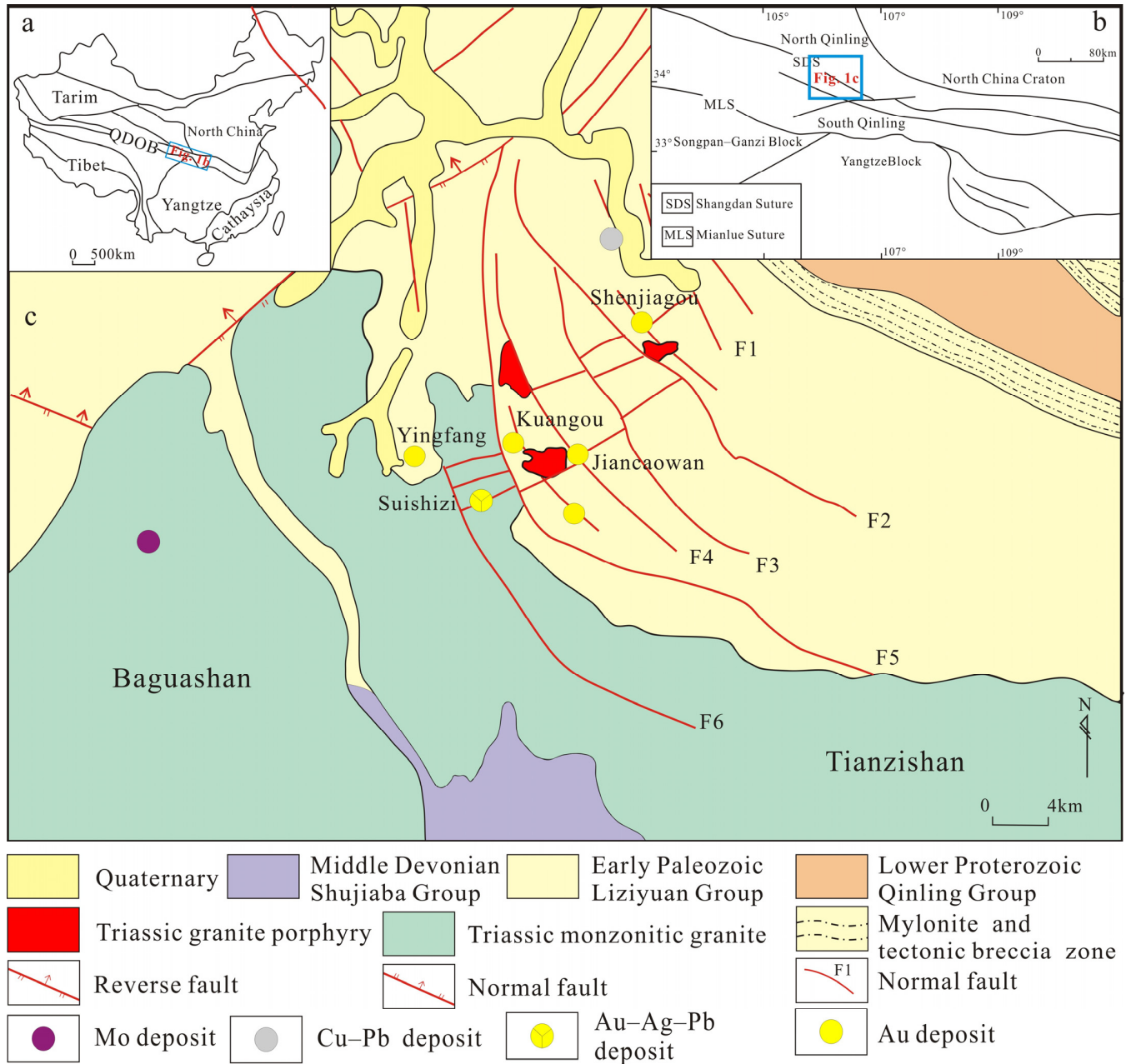

Figure 1. (**a**) Sketch map of China showing the location of the Qinling orogenic belt (QDOB, Qinling–Dabie Orogenic Belt). (**b**) Simplified tectonic map of the Qinling orogenic belt showing the location of the study area. (**c**) Simplified geological map of the Liziyuan area.

3. Geological Characteristics of Sections in the Liziyuan Area

3.1. Shenjiagou Section

The Shenjiagou section, in the eastern segment of the Liziyuan Au deposit, exposes strata of the Liziyuan Group of the ore-hosting horizon, which comprises chlorite schist, sericite–quartz schist interbedded with marble, chlorite–sericite–quartz schist interbedded with schistose limestone, and psammite. The section includes three Au orebodies (I–III) of

400–1000 m in length that are controlled by three parallel NW-trending brittle–ductile shear zones that played an important role in providing channels and spaces for ore-bearing fluids, with later-developed minor NE-trending structures having little effect on the orebodies. Intrusions in the mining area include rare lamprophyre and granodiorite dikes.

The Au mineralization occurs mainly within the brittle–ductile shear zones as quartz–sulfide veins (Figure 2a,b) containing pyrite, chalcopyrite, sphalerite, galena, arsenopyrite, and bismuthinite. Au grades range from 1 to 9 g t^{-1} (average 3 g t^{-1}). The highest Au contents and wall-rock alteration are concentrated in highly deformed zones. Mineralization zoning from the center to the edges of the section is characterized by banded silicification + planar metal sulfidation (Figure 2c), banded silicification + chloritization + disseminated metal sulfidation (Figure 2d), chloritization + epidotization + disseminated metal sulfidation, and chloritization + epidotization.
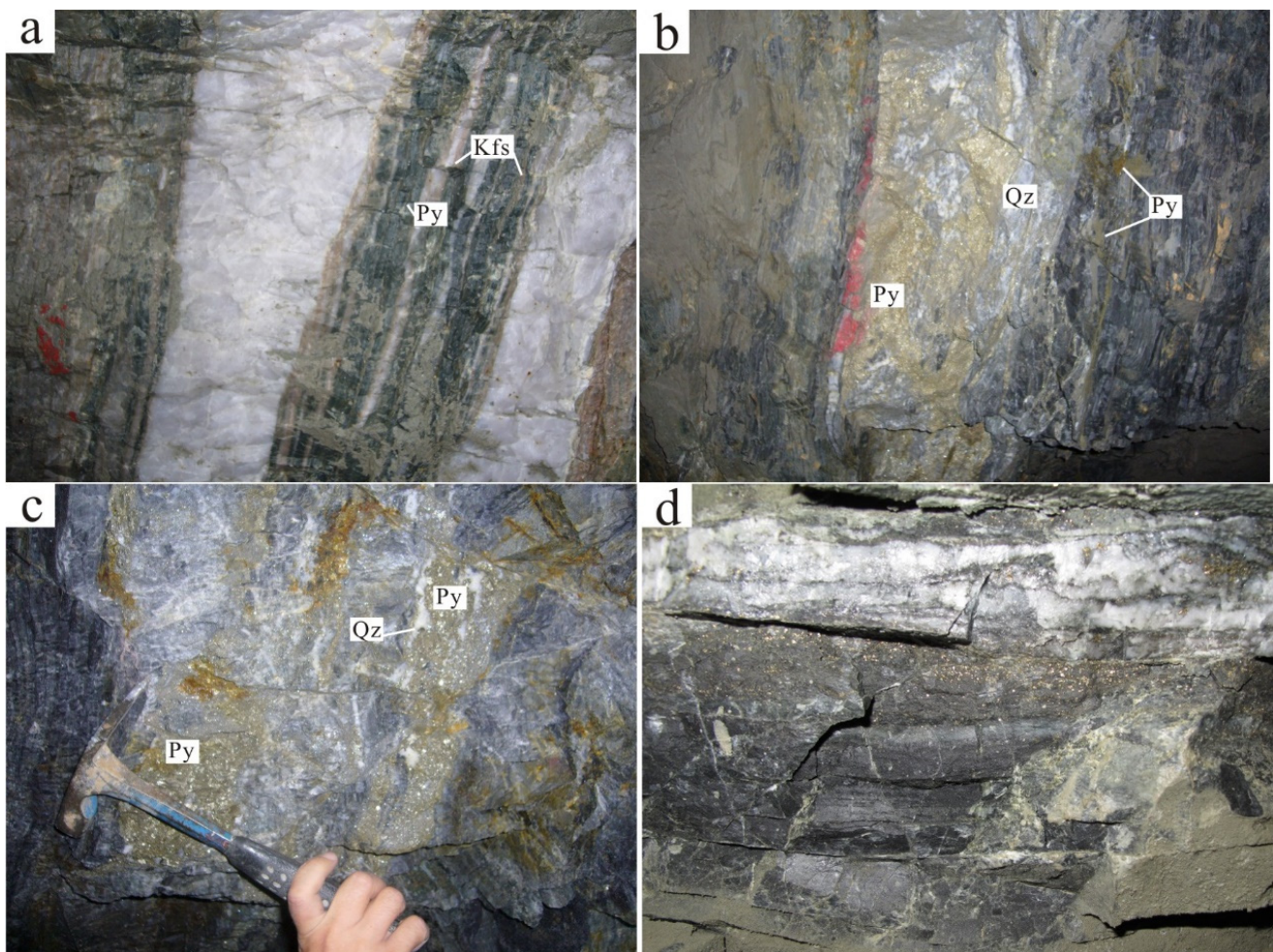

Figure 2. Ore and alteration styles of the Shenjiagou Au deposit. (**a**) Ore-bearing quartz–sulfide veins; (**b**) planar metal sulfidation in banded silicification; (**c**) planar metal sulfidation; and (**d**) disseminated metal sulfidation in banded silicification. Kfs, K-feldspar; Py, pyrite; Qz, quartz.

3.2. Suishizi Section

The Suishizi section, in the western segment of the Liziyuan Au deposit, comprises eight Au orebodies hosted in the Tianzishan intrusion. These orebodies are 1–6 m thick, and they are controlled by a group of NE- and E–W-trending fracture zones. Intrusions in the mining area include the Tianzishan monzogranite and mineralized diorite porphyrite.

The Au mineralization is hosted mainly by the diorite porphyrite (Figure 3a–c) and occurs as fractured and altered disseminated types containing considerable amounts of pyrite, chalcopyrite, sphalerite, arsenopyrite, native Au, electrum, native Ag, and petzite.

The boundaries between the fractured and altered disseminated orebodies and the host rocks are gradational. Au grades are 1–185 g t^{-1} (average 5.78 g t^{-1}) and Ag grades are 1–311 g t^{-1} (average 29.5 g t^{-1}). Mineralization zoning from the center to the edges of the section is characterized by silicification + metal sulfidation (Figure 3d) + sericitization (Figure 3e,f) + chloritization + carbonatization, potash feldspathization (Figure 3g)+ silicification, chloritization + epidotization + carbonatization (Figure 3h,i), and kaolinization + chloritization.
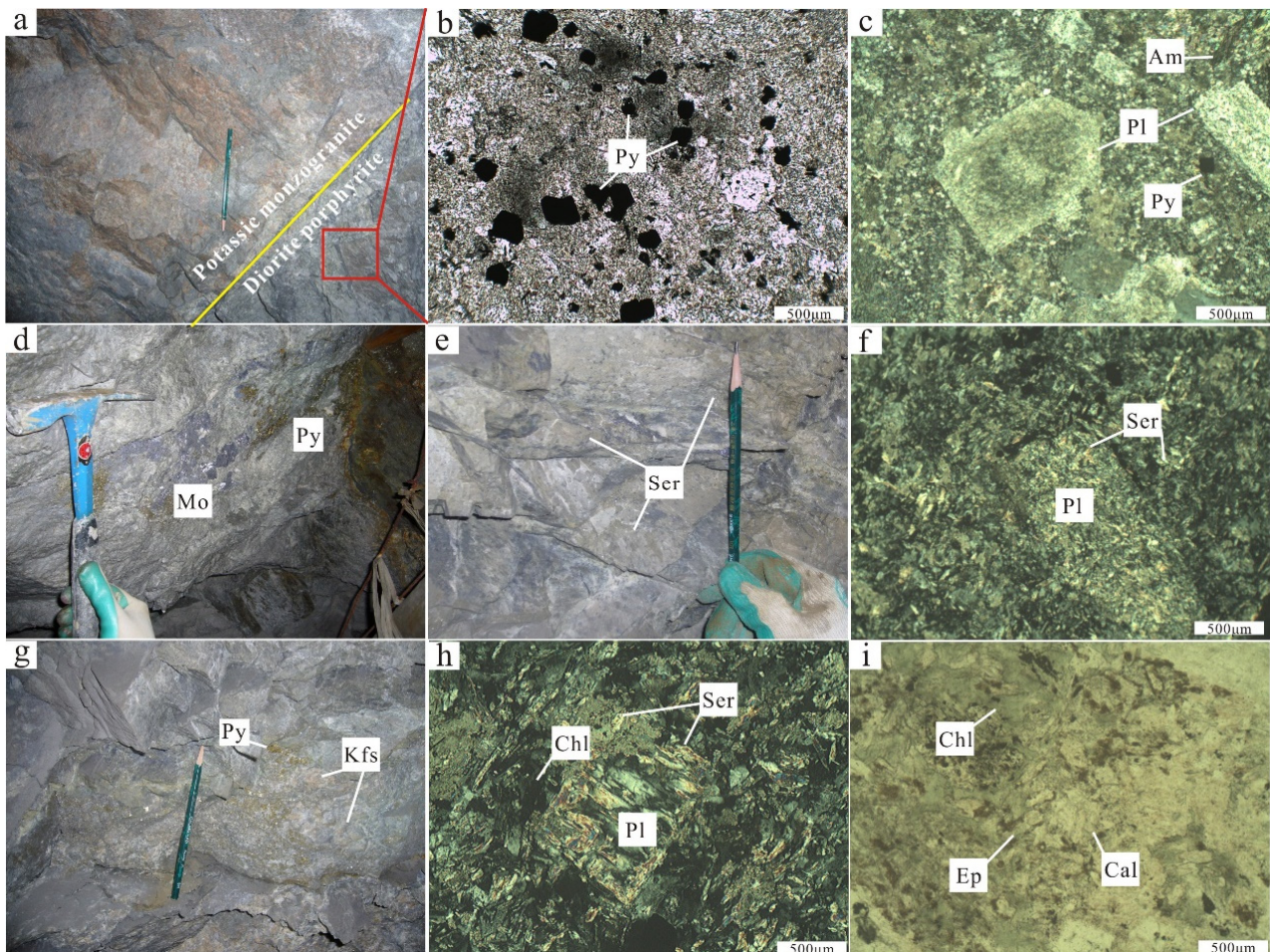

Figure 3. Ore and alteration styles of the Suishizi Au deposit. (**a**) Diorite porphyrite ore and surrounding monzogranite; (**b**) pyrites in diorite porphyrite ore; (**c**) pyrites and phenocrysts in diorite porphyrite ore; (**d**) metal sulfidation and silicification; (**e**,**f**) sericitization; (**g**) potash feldspathization + silicification; (**h**,**i**) chloritization + epidotization + carbonatization. Kfs, K-feldspar; Pl, Plagioclase; Am, Amphibole; Ser, sericite; Chl, chlorite; Cal, calcite; Ep, epidote; Py, pyrite; Mo, molybdenite.

3.3. Jiancaowan Section

The Jiancaowan section, in the central segment of the Liziyuan Au deposit, contains more than 30 echelon-type orebodies controlled by a group of NW- and NE-striking brittle–ductile shear zones and brittle faults, with the former being cut by the latter. The ore-bearing strata belong to the upper Liziyuan Group. On the western side of the mining area, intrusions comprise mainly the Triassic Tianzishan monzogranite and the Kuangou granite porphyry, with the latter being near the ore-bearing brittle–ductile shear zones. Quartz syenite, granodiorite, and diorite porphyrite dikes occur in the NE-trending faults.

The Au orebodies range in length from 10 to 80 m, with Au grades of 3–65 g t^{-1} (average 20 g t^{-1}). The Au mineralization occurs mainly within fracture zones in banded quartz–sulfide veins (Figure 4a) containing considerable amounts of pyrite, chalcopyrite,

sphalerite, and galena and in syn-deformational and syn-metamorphic quartz–K-feldspar veins (Figure 4b). Alteration zoning is characterized by strong silicification and sulfidation near orebodies. Based on mineral paragenetic assemblages and the cross-cutting relationships of ore-bearing veins, two stages of superimposed mineralization can be distinguished: an early stage characterized by syn-deformational quartz veins and banded quartz–pyrite mineralization, and a later stage of porphyry-type that overprints the earlier mineralization (Figure 4c), with these characterizing the Suizhizi Au deposit. In intensively fluid-superposed zones at the intersections between NW- and NE-striking brittle–ductile shear zones and brittle faults, alteration zoning from the center to the edges of the section is characterized by vein silicification + metal sulfidation (Figure 4d), silicification + chloritization + disseminated metal sulfidation (Figure 4e), and chloritization + epidotization (Figure 4f). In weakly fluid-superposed zones that are little affected by later stages of porphyry-type mineralization, alteration zoning is characterized by banded silicification + planar metal sulfidation, chloritization + epidotization + disseminated metal sulfidation, and chloritization + epidotization.
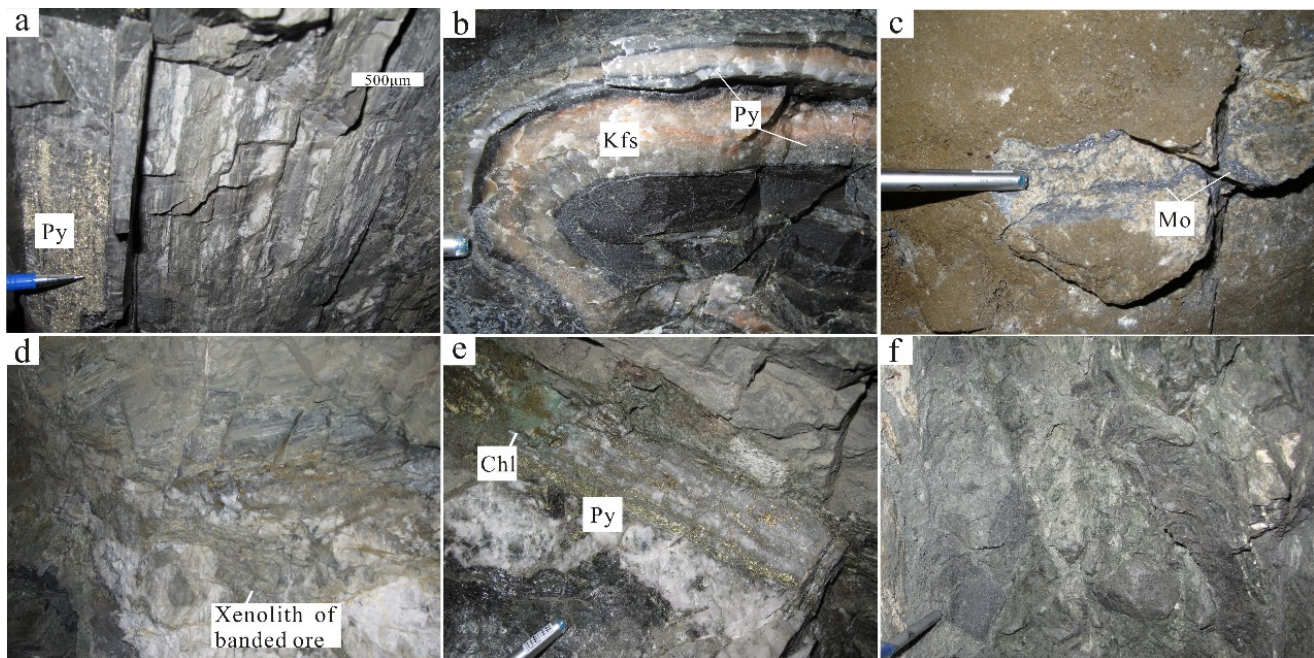

Figure 4. Ore and alteration styles in the Jiancaowan Au deposit. (**a**) Banded quartz–sulfide vein; (**b**) syn-deformational quartz–K-feldspar–sulfide vein; (**c**) porphyry-type mineralization; (**d**) early banded ore captured by a later quartz vein; (**e**) silicification + chloritization + disseminated metal sulfidation zone; (**f**) chloritization + epidotization zone. Kfs, K-feldspar; Chl, chlorite; Py, pyrite.

4. Metallogenetic Periods and Stages of the Liziyuan Au Deposit

Based on detailed field investigations and analysis of samples from the three sections of the Liziyuan Au deposit, two metallogenetic periods including five stages were identified. The early metallogenetic period (PI) is represented by quartz-vein and disseminated ores developed along NW-trending shear zones that formed in a compressional tectonic setting. This period can be further divided into two stages: an early syn-deformational quartz–pyrite vein stage (Stage I) with quartz and minor pyrite mineral associations, and a later banded quartz–polymetallic sulfide stage (Stage II) with quartz, pyrite, galena, and minor chalcopyrite and sphalerite. Syn-deformational quartz–K-feldspar–pyrite veins were developed locally in Stage II; these are similar in mineral composition to the Tianzishan monzogranite. Based on the spatiotemporal relationship between the mineralization and the intrusions, the Tianzishan magma probably provided the necessary magmatic fluids and heat for the mineralization in the Liziyuan gold deposit. The second metallogenetic

period (PII) includes porphyry-type mineralization that is represented by diorite porphyrite or granite porphyry-type orebodies. Porphyry-type mineralization is commonly developed in NE-trending brittle faults and overprints the NW-trending PI mineralization to form enriched orebodies. PII can be further divided into three stages, including a high-temperature stage (Stage III) with quartz, K-feldspar, pyrite, arsenopyrite and molybdenite mineral association; a mesothermal-high temperature stage (Stage IV) with quartz, pyrite, native gold, chalcopyrite, galena and sphalerite, and a late mesothermal-low temperature stage (Stage V) with kaolinite, chlorite, calcite, and minor metal sulfides.

In terms of spatial distribution, the Shenjiagou Au deposit was hosted in NW-trending ductile shear foliation with few diorite porphyrite or granite porphyry intrusions near the orebodies. The deposit formed mainly during the PI mineralization process, with PII mineralization being weakly superimposed. The Suishizi Au deposit was formed during PII mineralization and was hosted by the Tianzishan monzogranite, with mineralized NE-trending diorite porphyrite being the main Au-bearing orebody. Orebodies of the Jiancaowan Au deposit were distributed along NW-trending shear zones and NE-trending brittle faults, with dilational and enriched orebodies located at their intersection. The two periods of mineralization can be clearly distinguished in the Jiancaowan mining area.

5. Samples and Analytical Methods

Based on the close spatial relationship between intrusions and orebodies in the Liziyuan Au deposit, we chose seven Tianzishan monzogranite, five diorite porphyrite, and three granite porphyry dike samples from the surface and subsurface to investigate the relationship between mineralization and the tectonomagmatic evolution of the area. Whole-rock major- and trace-element contents were determined at the Key Laboratory of Western China's Mineral Resources and Geological Engineering, Ministry of Education, Chang'an University, Xi'an, China. Major-element contents were determined by X-ray fluorescence analysis of fused-glass disks, yielding analytical uncertainties of 1%–3%. Loss on ignition values were determined gravimetrically after heating at 980 °C for 30 min. Trace-element analyses involved inductively coupled plasma–mass spectrometry (ICP–MS; Agilent 7700e; Agilent Technologies (USA) Co., Ltd., Santa Clara, CA, USA). An internal standard was used to monitor instrumental drift, yielding uncertainties of 5%–10%, depending on the concentration.

Sulfur isotopic compositions of nine pyrite samples from quartz–pyrite veins in deposits in the Liziyuan Au deposit were determined at the Analytical Laboratory of the Beijing Research Institute of Uranium Geology (RIUG), Beijing, China. Samples were crushed to 200 mesh and mixed with cuprous oxide before heating at 980 °C at a pressure of 2×10^{-2} Pa to produce SO_2. The S isotopic compositions of the resulting SO_2 were determined by MS (MAT-251) yielding analytical precisions better than ±0.2‰. The isotopic compositions are reported relative to Vienna Cañon Diablo Troilite (V-CDT). In addition, 12 in situ isotope analyses of different ore types were undertaken at the State Key Laboratory of Continental Dynamics, Northwest University, Xi'an, China, using a 193 nm ArF excimer laser-ablation system (RESOlution M-50-LR, asi) coupled to an ICP–MS (Nu Plasma 1700), in high-resolution mode. A relatively low energy fluence of 3.5 J cm^{-2} was used, with an ablation frequency of 3 Hz, 25–30 μm spot size, and a single spot method. For correction of instrumental drift and mass bias, the standard–sample bracketing technique was used with repeated analyses of external standards before and after each sample. He was used as carrier gas and Ar as makeup gas. The methods used for in situ S isotope analyses of the sulfides have been described previously [49]). $\delta^{34}S$ values were normalized to V-CDT [50,51].

The H–O isotopic compositions of quartz-hosted fluid inclusions were determined at the RIUG using six representative quartz samples from quartz–pyrite veins. Pure monomineralic coarse-grained quartz samples were handpicked under a binocular microscope after crushing of selected samples, followed by fine grinding and sieving before treatment with dehydrated ethanol to remove remaining impurities. Oxygen isotope analyses involved 0.5 g of quartz of <200 mesh size, with O being extracted using the BrF$_5$ method described

by Clayton and Mayeda (1963) [52]. The resulting O_2 was reacted with graphite rods to produce CO_2 before analysis by isotope ratio MS (IRMS; MAT-253EM). Hydrogen isotope analyses involved ~3 g of quartz of <40–60 mesh size. Separated quartz grains were degassed of labile volatiles and secondary fluid inclusions by heating under vacuum at 200 °C for 3 h. The resulting H_2O was reduced by reaction with Zn metal in a sealed tube at 450 °C [53]). Hydrogen isotopic compositions were determined by IRMS, as for the O analyses.

$\delta^{18}O$ and δD values are reported relative to Vienna Standard Mean Ocean Water (V_{SMOW}) with analytical precisions of ± 0.2‰. Isotopic fractionation of O between quartz and water was determined using the equations of Zheng (1993) [54].

Zircons from the Tianzishan monzogranite were selected for sensitive high-resolution ion-microprobe (SHRIMP II) U-Pb dating at the Beijing SHRIMP Center, Institute of Geology, Chinese Academy of Geological Sciences (CAGS), Beijing, China. Cathodoluminescence (CL) images were collected using polished zircons prior to U–Th–Pb analyses to display internal textures and to guide SHRIMP analyses. Common-Pb correction used the ^{204}Pb method of Compston et al. (1984) [55]. The methodology has been described in detail by Compston et al. (1992) [56] and Williams (1998) [57]. Errors are quoted at the 1σ level, except for weighted mean ages, which are quoted at the 2σ level. Data processing was carried out using Isoplot v. 2.49 (Ludwig, 2003) [58].

Fourteen pyrite samples were separated from three ore samples for Rb–Sr dating. After crushing to 40–60 mesh, individual pyrite grains were handpicked under a binocular microscope to achieve >99% purity. Selected samples were rinsed repeatedly with distilled water, dried, and crushed to <200 mesh size. Powders (200 mg) from each sulfide sample were digested with HF–HNO_3 in Teflon beakers. After evaporation and re-dissolution, the Rb–Sr dating was undertaken by thermal ionization MS (TIMS; GV Isoprobe-T) at the RIUG. Analyses of the US National Institute of Standards and Technology (NIST) Standard Reference Material NBS987 yielded $^{87}Sr/^{86}Sr = 0.71025 \pm 0.00007$. A $^{86}Sr/^{88}Sr$ ratio of 0.1194 was used to correct for instrumental fractionation.

6. Results

6.1. Major Elements

The seven Tianzishan monzogranite samples had major-oxide contents as follows: SiO_2 = 69.50–73.52 wt.%; K_2O = 4.45–6.07 wt.%; Na_2O = 3.20–4.49 wt.%; Al_2O_3 = 13.98–14.95 wt.%; CaO = 0.27–2.27 wt.%; Fe_2O_3 = 0.28–0.83 wt.%; FeO = 0.35–1.45 wt.%; MgO = 0.14–0.63 wt.%; TiO_2 = 0.09–0.25 wt.%, and P_2O_5 = 0.03–0.10 wt.% (Table 1), with $Al_2O_3/(CaO + Na_2O + K_2O)$ (A/CNK) ratios of 0.91–1.15. These samples belong to the subalkaline (Figure 5a), high-K to shoshonitic (Figure 5b), and metaluminous to peraluminous series (Figure 5c).
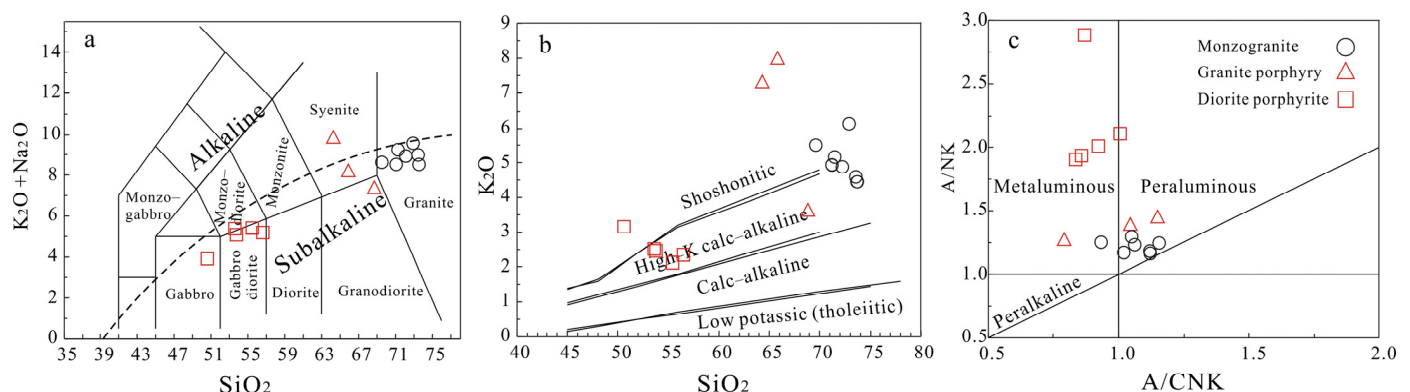

Figure 5. (**a**) SiO_2–($Na_2O + K_2O$); (**b**) SiO_2–K_2O; and (**c**) (A/NK)–(A/CNK) diagrams for the monzogranite, granite porphyry, and diorite porphyrite.

Table 1. Major element contents (wt %) trace and rare earth element concentrations (ppm) of Tianzishan monzogranite, diorite porphyrite and granite porphyry dikes.

Sample No.	TZ1	TZ2	TZ3	TZ4	TZ5	TZ6	TZ7	SZ1	SZ2	SZ3	SZ4	SZ5	JC1	JC2	JC3
Lithology				Monzogranite						Diorite Porphyrite				Granite Porphyry	
SiO_2	72.82	71.11	73.52	73.47	72.15	71.36	69.5	50.59	53.74	53.57	56.45	55.38	68.7	64.24	65.89
TiO_2	0.15	0.09	0.13	0.12	0.25	0.16	0.11	0.84	0.88	0.58	0.69	1.07	0.34	0.4	0.11
Al_2O_3	14.43	14.64	14.25	14.44	14.95	14.43	13.98	13.57	14.9	14.3	14.7	14.97	15.07	17.07	11.52
Fe_2O_3	0.77	0.29	0.54	0.52	0.56	0.83	0.67	3.03	3.21	2.32	1.57	2.9	1.08	1.08	0.91
FeO	0.78	1.46	0.38	0.37	0.89	0.35	0.92	3.82	2.85	4.31	4.26	3.82	1.41	1.12	1.12
MnO	0.09	0.05	0.04	0.03	0.04	0.04	0.11	0.19	0.14	0.16	0.1	0.13	0.06	0.06	0.05
MgO	0.25	0.26	0.18	0.14	0.63	0.26	0.53	7.53	7.1	7.8	6.57	5.87	1.18	1.28	2.54
CaO	0.27	1.43	1.02	0.32	0.51	0.98	2.27	6.02	4.31	5.16	4.76	5.55	1.62	2.27	3.06
Na_2O	4.49	3.69	4.11	4.49	4.13	4.16	3.2	0.8	2.68	2.85	2.9	3.38	3.88	2.68	0.29
K_2O	6.07	4.88	4.45	4.55	4.84	5.12	5.46	3.12	2.44	2.49	2.33	2.11	3.57	7.22	7.88
P_2O_5	0.06	0.05	0.03	0.03	0.1	0.05	0.05	0.31	0.35	0.14	0.1	0.32	0.09	0.17	0.08
LOI	0.98	1.79	0.97	0.81	0.95	1.84	3.32	9.52	6.72	6.45	5.32	4.02	2.54	2.58	6.09
TOTAL	100.22	99.73	99.61	99.3	100.01	99.6	100.1	99.34	99.31	100.13	99.75	99.5	99.55	100.17	99.54
A/CNK	1.12	1.05	1.06	1.12	1.15	1.02	0.91	0.87	1.00	0.85	0.92	0.84	1.14	1.04	0.79
A/NK	1.16	1.29	1.23	1.17	1.24	1.16	1.25	2.89	2.11	1.93	2.01	1.91	1.47	1.39	1.28
La	12.97	47.55	19.05	18.2	18.14	16.86	41.72	52.23	55.93	19.12	17.19	22.88	36.69	69.9	10.64
Ce	32.39	90.3	31.88	27.23	36.05	33.5	76.49	97.58	103.3	38.54	29.54	41.71	68.7	124.9	18.84
Pr	2.22	9.88	3.49	3.13	3.11	4.08	8.33	11.08	11.46	4.31	3.6	4.76	8.21	12.91	1.91
Nd	7.54	33.55	11.79	10.11	10.66	14.59	28.46	39.57	40.82	17.52	13.78	16.95	30.4	46.2	6.64
Sm	1.11	5.39	1.91	1.58	1.71	2.47	4.61	6.4	6.47	3.31	2.83	2.86	5.4	6.79	1.01
Eu	0.32	0.95	0.55	0.4	0.56	0.71	0.97	1.64	1.76	1.06	0.86	0.75	1.59	2.01	0.29
Gd	0.79	4.06	1.35	1.16	1.19	1.78	3.72	5.19	5.08	3.3	2.82	2.44	4.51	7	0.8
Tb	0.08	0.59	0.17	0.17	0.17	0.22	0.57	0.7	0.72	0.42	0.45	0.37	0.64	0.61	0.07
Dy	0.42	3.3	0.88	0.88	0.91	1.12	3.41	4.11	4.1	2.41	2.68	2.13	3.62	2.89	0.33
Ho	0.08	0.58	0.14	0.14	0.14	0.19	0.64	0.76	0.74	0.49	0.5	0.4	0.66	0.48	0.05
Er	0.22	1.61	0.39	0.36	0.39	0.51	1.79	2.06	1.99	1.38	1.37	1.1	1.71	1.31	0.16
Tm	0.03	0.26	0.06	0.05	0.06	0.07	0.31	0.33	0.32	0.2	0.22	0.19	0.26	0.16	0.02
Yb	0.18	1.73	0.42	0.31	0.4	0.49	2.04	2.11	2.08	1.21	1.41	1.26	1.66	1.04	0.12
Lu	0.03	0.28	0.07	0.05	0.06	0.08	0.33	0.33	0.33	0.18	0.23	0.19	0.26	0.14	0.02
Y	1.52	17.74	4.68	4.11	4.09	5.94	19.18	20.31	20.21	10.96	13.2	11.47	17.26	11.05	1.16
ΣREE	58.36	200	72.15	63.77	73.55	76.66	173	224	235	93.44	77.48	97.99	164	276	40.9
LREE	56.54	187.62	68.67	60.65	70.23	72.21	160.58	208.5	219.74	83.86	67.8	89.91	150.99	262.7	39.33
HREE	1.83	12.41	3.48	3.12	3.31	4.46	12.8	15.59	15.36	9.57	9.68	8.07	13.32	13.63	1.57
LREE	30.98	15.12	19.74	19.42	21.21	16.2	12.54	13.38	14.3	8.76	7.01	11.13	11.33	19.28	25.04
La_N/Yb_N	48.42	18.53	30.65	39.08	30.73	23.13	13.81	16.71	18.13	10.7	8.24	12.24	14.97	45.55	58.93
δEu	0.99	0.6	0.99	0.86	1.15	0.98	0.69	0.84	0.9	0.97	0.92	0.85	0.96	0.88	0.94
Rb	131	152	152	125	116	121	155	111	116	116	104	115	70	146	206
Ba	1377	1083	1227	1343	1947	1910	1378	656	1052	785.1	582	1094	1224	2510	1107
Th	15.29	17.53	11.14	10.34	8.29	11.78	18.11	13.17	14.64	9.61	5.59	8.33	8.62	56.4	7.021
U	4.03	12.271	7.798	7.238	5.803	8.246	12.677	9.219	10.248	3.911	3.913	5.831	6.034	18.1	2.756
K	50,368	40,494	36,926	37,755	40,162	42,485	45,306	25,889	20,247	20,662	19,334	29,623	17,509	59,911	65,387
Ta	0.681	1.84	0.63	0.62	0.62	0.55	1.83	1.54	1.72	0.61	0.68	1.21	1.16	0.773	0.482
Nb	9.081	20	8.8	4.8	9.5	8.7	17.9	25.5	28.6	8.39	8.4	15.4	15.4	10.91	6.091
Sr	274.5	272	512	584	702	652	256	717	974	724.2	445	416	752	531.9	178.9
Nd	7.539	33.55	11.79	10.11	10.66	14.59	28.46	39.57	40.82	17.52	13.78	16.95	30.4	46.2	6.644
P	261.8	218.2	130.9	130.9	436.4	218.2	218.2	1353	1527	610.9	436.4	392.7	1396	741.8	349.1
Zr	126.6	190	108	110	181	130	173	176	194	111.8	120	142	186	275.6	79.32
Hf	3.597	5.66	3.33	3.08	4.76	3.84	4.58	3.5	3.92	2.867	2.83	4.09	3.77	6.612	2.483
Sm	1.106	5.39	1.91	1.58	1.71	2.47	4.61	6.4	6.47	3.31	2.83	2.86	5.4	6.786	1.007
Ti	899.2	539.5	779.3	719.4	1499	959.2	659.4	5036	5276	3477	4137	2038	6415	2398	659.4

The diorite porphyrite dikes of the Suishizi Au mine had major-oxide contents of SiO_2 = 50.59–56.45 wt.%; K_2O = 2.11–3.12 wt.%; Na_2O = 0.80–3.30 wt.%; Al_2O_3 = 13.57–14.97 wt.%; CaO = 4.31–6.02 wt.%; Fe_2O_3 = 1.57–3.21 wt.%; FeO = 2.85–4.31 wt.%; MgO = 5.87–7.53 wt.%; TiO_2 = 0.58–1.07 wt.%, and P_2O_5 = 0.10–0.35 wt.%, with A/CNK = 0.85–1.00. These samples are subalkaline (Figure 5a), high-K to shoshonitic (Figure 5b), and metaluminous (Figure 5c).

The granite porphyry dikes coexisting with the diorite porphyrite dikes had higher SiO_2 (64.24–68.70 wt.%) and Al_2O_3 (11.52–17.07 wt.%) contents, lower Fe_2O_3 (0.91–1.08 wt.%), FeO (1.12–1.41 wt.%), MgO (1.18–2.54 wt.%), TiO_2 (0.11–0.40 wt.%), and P_2O_5 (0.08–0.17 wt.%) contents, and K_2O = 3.57–7.88 wt.%, and Na_2O = 0.29–3.88 wt.%, with A/CNK = 0.79–1.14.

These dikes are subalkaline to alkaline (Figure 5a), high-K to shoshonitic (Figure 5b), and metaluminous to peraluminous (Figure 5c).

6.2. Trace Elements

The Tianzishan monzogranite is enriched in light rare earth elements (LREEs), Zr, and Hf, depleted in heavy REEs (HREEs), Nb, Ti, and P, and has negative to small positive Eu anomalies (Eu/Eu* = 0.60–1.15; Figure 6a). The diorite porphyrite and granite porphyry dikes are similarly enriched in LREEs, with $(La/Yb)_N$ ratios of 8.24–18.13 and 14.97–58.93 and negative Eu anomalies (Eu/Eu* = 0.84–0.97 and 0.88–0.96), respectively. The primitive mantle-normalized trace-element diagram (Figure 6b) indicates positive Zr and Hf anomalies and negative Nb, P, and Ti anomalies.
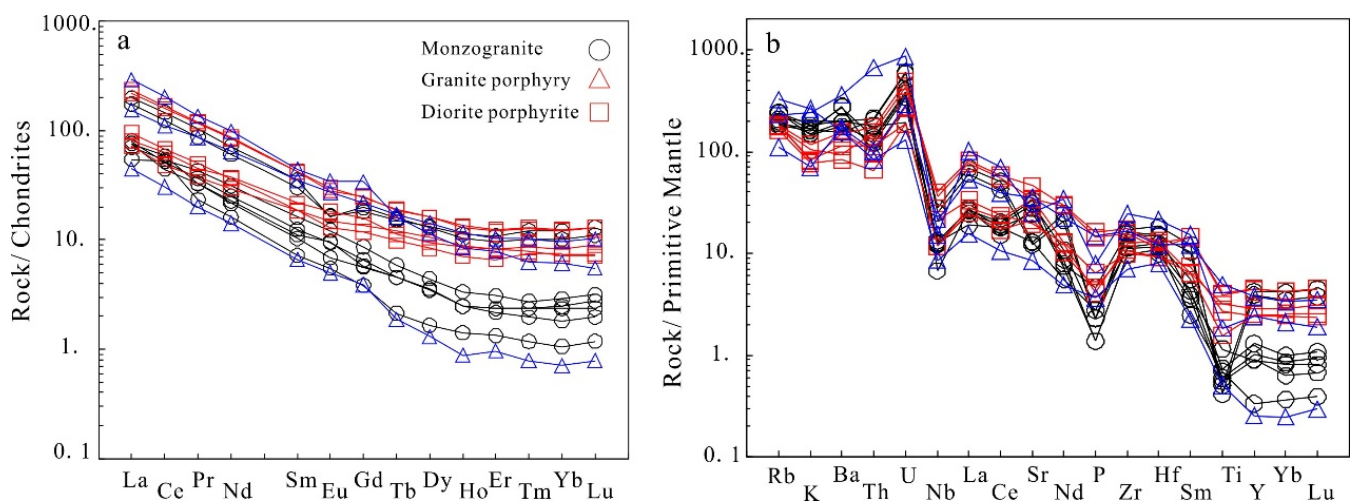
Figure 6. (**a**) Chondrite-normalized REE patterns; and (**b**) primitive mantle-normalized multi-element diagrams for the monzogranite, granite porphyry, and diorite porphyrite.

6.3. Sulfur Isotopes

The pyrite δ^{34}S values of ore-bearing diorite porphyrite of the Suishizi Au deposit, banded quartz–sulfide veins from the Shenjiagou Au deposit, and ore-bearing quartz veins of the Jiancaowan Au deposit were 7.28‰–7.91‰ (average of 7.62‰), −4.95‰ to −2.44‰ (average −3.91‰), and 1.79‰–1.89‰ (average 1.83‰), respectively (Table 2).

Table 2. Single mineral and in situ sulfur isotope of pyrite from Liziyuan gold deposit.

Sample No.	Section	Host Rock	$\delta^{34}S_{VCDT}$(‰)	Test Method
JCS1	Jiancaowan	Quartz vein	7.04	In-situ analysis
JCS2	Jiancaowan	Quartz vein	7.96	In-situ analysis
JCS3	Jiancaowan	Quartz vein	9.12	In-situ analysis
JCS4	Jiancaowan	Quartz vein	1.79	In-situ analysis
JCS5	Jiancaowan	Quartz vein	2.11	In-situ analysis
JCS6	Jiancaowan	Quartz vein	1.75	In-situ analysis
JCS7	Jiancaowan	Quartz vein	0.10	In-situ analysis
JCS8	Jiancaowan	Quartz vein	3.08	In-situ analysis
JCS9	Jiancaowan	Quartz vein	1.43	In-situ analysis
JCW-S1	Jiancaowan	Quartz vein	1.89	Single mineral analysis
JCW-S2	Jiancaowan	Quartz vein	1.82	Single mineral analysis
JCW-S3	Jiancaowan	Quartz vein	1.79	Single mineral analysis
SSI1	Suishizi	Diorite porphyrite	7.39	In-situ analysis
SSI2	Suishizi	Diorite porphyrite	7.13	In-situ analysis
SSI3	Suishizi	Diorite porphyrite	7.58	In-situ analysis
SS01	Suishizi	Diorite porphyrite	7.91	Single mineral analysis
SS02	Suishizi	Diorite porphyrite	7.89	Single mineral analysis

Table 2. *Cont.*

Sample No.	Section	Host Rock	$\delta^{34}S_{VCDT}$(‰)	Test Method
SS03	Suishizi	Diorite porphyrite	7.84	Single mineral analysis
SS04	Suishizi	Diorite porphyrite	7.77	Single mineral analysis
SS05	Suishizi	Diorite porphyrite	7.69	Single mineral analysis
SS06	Suishizi	Diorite porphyrite	7.58	Single mineral analysis
SS07	Suishizi	Diorite porphyrite	7.49	Single mineral analysis
SS08	Suishizi	Diorite porphyrite	7.45	Single mineral analysis
SS09	Suishizi	Diorite porphyrite	7.29	Single mineral analysis
SS10	Suishizi	Diorite porphyrite	7.28	Single mineral analysis
SJ01	Shenjiagou	Banded quartz-sulfide vein	−2.44	Single mineral analysis
SJ02	Shenjiagou	Banded quartz-sulfide vein	−2.58	Single mineral analysis
SJ03	Shenjiagou	Banded quartz-sulfide vein	−4.13	Single mineral analysis
SJ04	Shenjiagou	Banded quartz-sulfide vein	−4.44	Single mineral analysis
SJ05	Shenjiagou	Banded quartz-sulfide vein	−4.91	Single mineral analysis
SJ06	Shenjiagou	Banded quartz-sulfide vein	−4.95	Single mineral analysis

The in situ δ^{34}S values of pyrites from the Suishizi section and quartz veins of the Jiancaowan Au deposit were 7.04‰–9.12‰ (average 7.70‰) and 0.10‰–3.08‰ (average 1.71‰), respectively.

6.4. Oxygen and Hydrogen Isotopes

The O–H isotopic data for fluid inclusions in 14 quartz samples from three deposits are listed in Table 3. All samples are from Stage IV, which was characterized by abundant sulfide precipitation as a result of the fluid present during the major ore-forming stage and the composition of its source. The δD values of quartz vein samples from the Suishizi, Jiancaowan, and Shenjiagou sections were −80‰ to −75‰, −92‰ to −82‰, and −93 to −87‰, respectively, and the $\delta^{18}O_{water}$ values are 3.07‰–3.98‰, 1.67‰–5.24‰, and −0.03‰ to 1.37‰, respectively.

Table 3. δ^{18}O and δD values for Liziyuan gold deposit.

Sample No.	Section	Mineral	$\delta D_{V\text{-}SMOW}$(‰)	$\delta^{18}O_{V\text{-}SMOW}$(‰)	$\delta^{18}O_{water}$(‰)	Th (°C)
SS001	Suishizi	Quartz	−75	10.16	3.62	310
SS002	Suishizi	Quartz	−80	9.72	3.18	310
SS003	Suishizi	Quartz	−79	9.65	3.11	310
SS004	Suishizi	Quartz	−75	9.61	3.07	310
SS005	Suishizi	Quartz	−78	10.12	3.58	310
SS006	Suishizi	Quartz	−78	9.98	3.44	310
SS007	Suishizi	Quartz	−76	9.76	3.22	310
SS008	Suishizi	Quartz	−79	10.52	3.98	310
JC004	Jiancaowan	Quartz	−84	12.1	1.37	216
JC005	Jiancaowan	Quartz	−82	11.1	−1.33	189
JC006	Jiancaowan	Quartz	−92	12.4	−0.03	189
SJ001	Shenjiagou	Quartz	−89	12.5	5.24	290
SJ002	Shenjiagou	Quartz	−93	12.1	4.84	290
SJ003	Shenjiagou	Quartz	−87	12.4	1.67	216

6.5. Zircon U-Pb Geochronology

Zircon grains from the Tianzishan monzogranite are subhedral–euhedral, stubby or elongated, and 100–200 μm long. In CL images, magmatic cores display oscillatory zoning or are homogeneous (Figure 7). Seven analyses were performed on seven grains. Seven analyses of magmatic domains yielded U contents of 262–2959 ppm and Th/U ratios of 0.20–0.61 (Table 4), with the seven analyses yielding a weighted mean ^{206}Pb/^{208}Pb age of 236.1 ± 1.9 Ma (MSWD = 0.95; Figure 7).
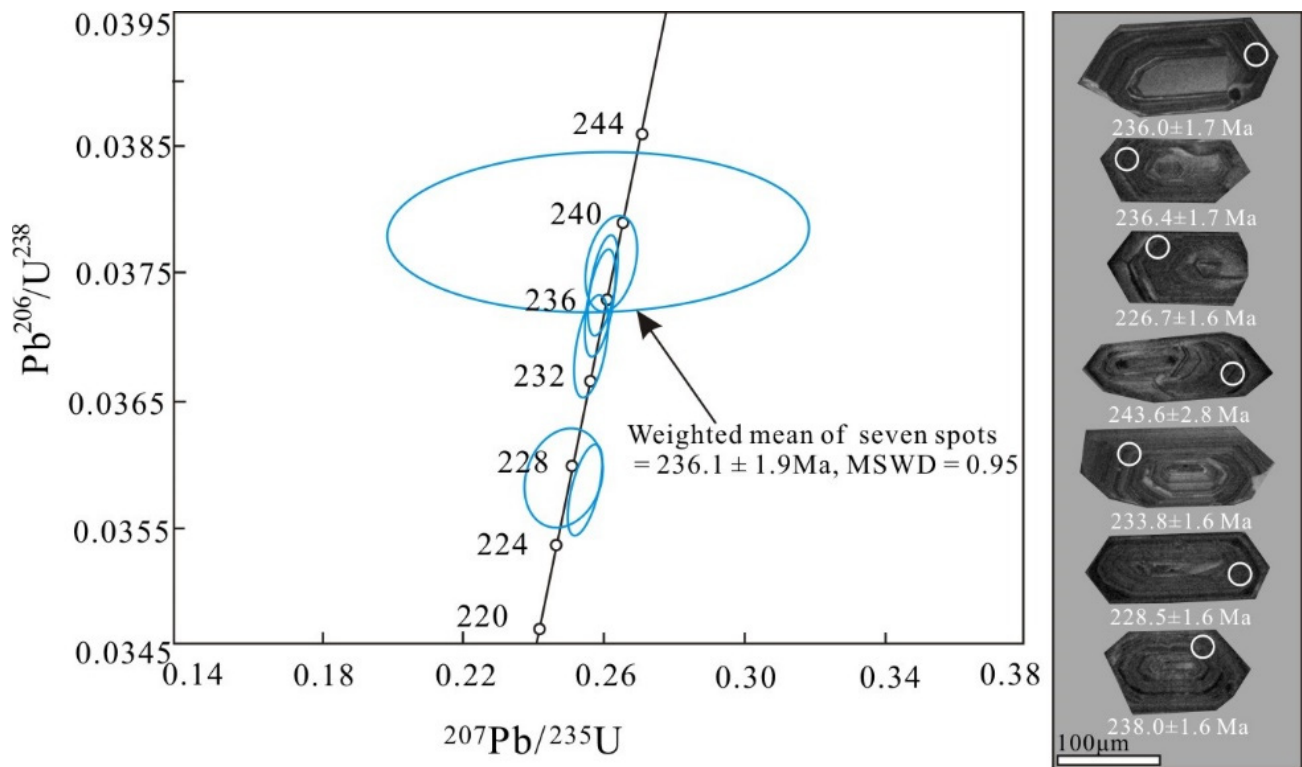
Figure 7. SHRIMP U-Pb Concordia diagram and CL images of zircons from the Tianzishan monzogranite.

Table 4. SHRIMP zircon U-Pb dating of the Tianzishan monzogranite.

Spot	^{206}Pb (%)	U ($\times 10^{-6}$)	Th	$^{232}Th/^{238}U$	$^{206}Pb^*$ $\times 10^{-6}$	$t(^{206}Pb/^{238}U)$ (Ma)	$^{207}Pb/^{235}U$ Ratio	1σ	$^{206}Pb/^{238}U$ Ratio	1σ
C005.1	1.23	2067	602	0.3	64.5	228.5 ± 1.6	0.2722	2.7	0.03609	0.73
C005.2	0.67	2959	578	0.2	96.1	238.0 ± 1.6	0.269	2	0.03761	0.68
C005.3	0.16	1537	406	0.27	49.2	236.0 ± 1.7	0.2639	1.4	0.03728	0.75
C005.4	0.22	2624	1097	0.43	84.4	236.4 ± 1.7	0.2586	1.8	0.03736	0.71
C005.7	0.23	1966	814	0.43	60.5	226.7 ± 1.6	0.2591	1.3	0.03579	0.7
C005.8	0.21	2577	771	0.31	81.9	233.8 ± 1.6	0.2607	1.4	0.03693	0.7
C005.9	2.66	262	156	0.61	8.73	243.6 ± 2.8	0.345	11	0.03852	1.2

6.6. Rb–Sr Dating of Pyrite

The results of Rb–Sr isotope analysis of the 14 pyrite samples from banded silicification (Figure 8a), diorite porphyrite (Figure 8b), and quartz vein (Figure 8c) type ores are shown in Table 5. The samples had variable concentrations of Rb (0.41–13.1 ppm) and Sr (2.29–36.7 ppm), which yielded variable $^{87}Rb/^{86}Sr$ (0.1347–5.1663) and $^{87}Sr/^{86}Sr$ (0.7071–0.7216) ratios. Fourteen pyrite samples yielded three well-defined isochrons with ages of 220 ± 7.5 Ma (MSWD = 1.8) with initial $^{87}Sr/^{86}Sr$ (($^{87}Sr/^{86}Sr)_i$) = 0.70693 ± 0.0002, 205.8 ± 8.7 Ma (MSWD = 1.07) with ($^{87}Sr/^{86}Sr)_i$ = 0.70720 ± 0.00022, and 199 ± 15 Ma (MSWD = 1.8) with ($^{87}Sr/^{86}Sr)_i$ = 0.70715 ± 0.00063.

Table 5. Rb-Sr isotopic dating of pyrite samples from Liziyuan gold deposit.

Sample No.	Object	Rb (ppm)	Sr (ppm)	$^{87}Rb/^{86}Sr$	$^{87}Sr/^{86}Sr$	Std Err	Section	Host Rock
Bh052	Pyrite	1.78	6.83	0.7544	0.709184	0.000016	Shenjiagou	Banded silicification
Bh043	Pyrite	5.67	4.94	3.3233	0.717372	0.000018	Shenjiagou	Banded silicification

Table 5. *Cont.*

Sample No.	Object	Rb (ppm)	Sr (ppm)	^{87}Rb/^{86}Sr	^{87}Sr/^{86}Sr	Std Err	Section	Host Rock
Bh055	Pyrite	0.955	9.31	0.1915	0.707724	0.000011	Shenjiagou	Banded silicification
Bh056/Bh042	Pyrite	0.414	6.26	0.9823	0.709863	0.000016	Shenjiagou	Banded silicification
Bh011	Pyrite	9.21	9.51	2.8023	0.715608	0.000009	Suishizi	Diorite porphyrite
Bh030	Pyrite	12.4	23.3	1.5426	0.711535	0.000009	Suishizi	Diorite porphyrite
Bh038	Pyrite	3.52	34.8	0.2929	0.708111	0.000017	Suishizi	Diorite porphyrite
Bh036	Pyrite	7.65	36.7	0.6023	0.708854	0.000013	Suishizi	Diorite porphyrite
Bh037	Pyrite	19.1	20.3	2.7210	0.715068	0.000018	Suishizi	Diorite porphyrite
Bh068-1	Pyrite	7.51	161	0.1347	0.707746	0.000018	Suishizi	Diorite porphyrite
Bh054	Pyrite	1.32	3.1	1.2375	0.710981	0.000011	Jiancaowan	Quartz vein
Bh045	Pyrite	2.76	3.97	2.0100	0.713257	0.000017	Jiancaowan	Quartz vein
Bh044	Pyrite	4.08	2.29	5.1663	0.721561	0.000017	Jiancaowan	Quartz vein
Bh051	Pyrite	0.671	10.9	0.1784	0.707115	0.000017	Jiancaowan	Quartz vein
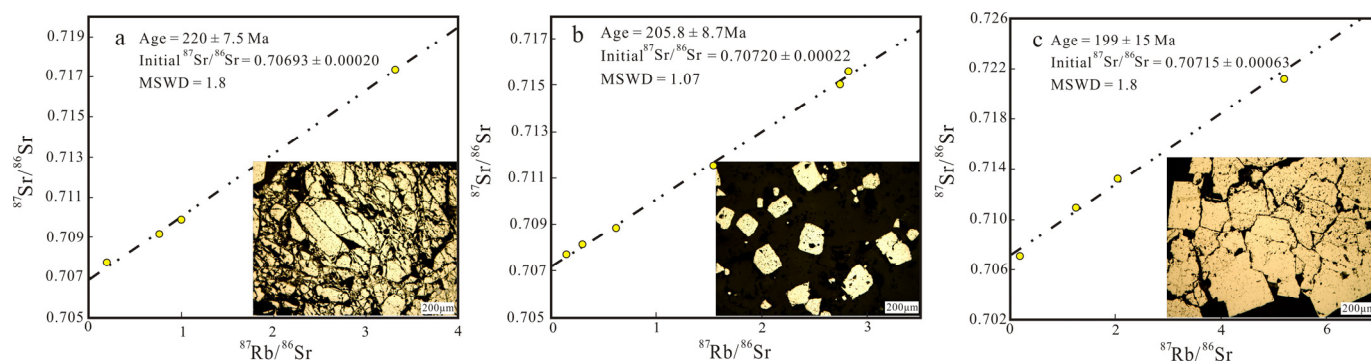
Figure 8. Rb–Sr isochrons of pyrite from banded silicification (**a**), diorite porphyrite (**b**), and quartz veins (**c**).

7. Discussion

7.1. Timing of Magmatism and Mineralization

The relationship between mineralization and magmatism in the Liziyuan Au deposit is poorly understood, with some studies supporting mineralization being related to magmatic activity (e.g., the Tianzishan intrusion, [59,60]), and others preferring suggesting that there is no genetic relationship between Au deposition and magmatism [61,62]. The Liziyuan Au deposit provides an opportunity to determine whether orogenic Au deposits are related to magmatism in the WQOB [63–67].

To explore the possible relationship between mineralization and magmatism in the Liziyuan Au deposit, pyrites from ores and zircons from the Tianzishan monzogranite were dated to identify temporal coupling between magmatism and hydrothermal activity. Pyrite is one of the most common sulfide minerals in the Liziyuan Au deposit, and pyrite Rb–Sr dating is a widely used technique [68–70]. In this deposit, pyrite commonly occurs in subhedral–anhedral forms in banded quartz veins and as subhedral–euhedral granules in ore-bearing diorite porphyrite and quartz veins. To ensure reliable determination of the mineralization age, we selected pyrites that formed coevally with the three types of ore and were undisturbed by later fluids for analysis. The Rb–Sr isochron age of pyrite from banded quartz veins in the Shenjiagou section is 220.5 ± 7.5 Ma, and those for subhedral–euhedral

granular pyrite from ore-bearing diorite porphyrite and quartz veins in the Suishizi section were 205.8 ± 8.7 and 199 ± 15 Ma, respectively. The Rb–Sr ages of the Au-bearing pyrite samples were considered reliable (Figure 8). The lack of covariance between the 1/Sr values and ^{87}Rb/^{86}Sr ratios of the samples (Figure 9) indicates that the isochron age has isochronal meaning [71], implying a homogenous and closed isotopic system [72]. The calculated ages thus reflect the metallogenic age of the two types of Au mineralization, i.e., the earlier metamorphic metallogenic period (220.5 Ma) and the later magmatic metallogenic period (205–199 Ma). The Tianzishan monzogranite yielded an age of 236.1 ± 1.9 Ma, which represents a new minimum age of formation (256.1 ± 3.7 Ma [73]; 241.3 ± 1.2 Ma [62]; 241 ± 1.7 Ma [74]). Our previously published ages for the ore-bearing diorite porphyrite and granite porphyry were 212.2 ± 1.2 and 213.9 ± 0.7 Ma [75].
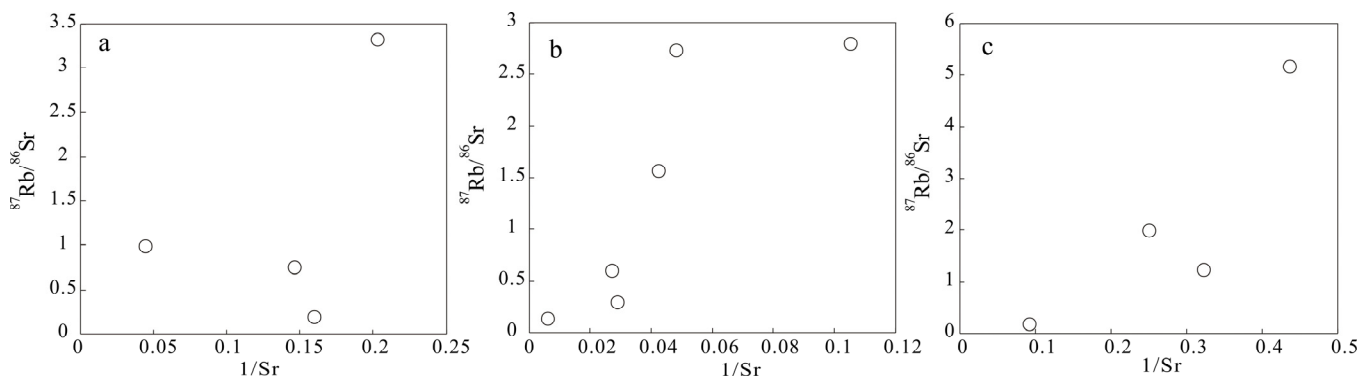
Figure 9. (^{87}Sr/^{86}Sr)–(1/Sr) diagrams for the pyrites from banded silicification (**a**), diorite porphyrite (**b**), and quartz veins (**c**) (modified after Li et al., 2002 [76]).

The two emplacement ages of the intrusions that are closely spatially related to the Au orebodies (236.1 and 213.9–212.2 Ma) predated the two Au mineralization periods (220.5 and 206–199 Ma) by 5–10 Myr, corresponding to the time interval of fluid exsolution from the melt [77,78]. There is thus close temporospatial coupling between mineralization and magmatic fluid activity.

7.2. Source of the Metallogenic Material

Many studies have used H–O–S isotope analyses to elucidate ore genesis in different types of Au deposit, with H–O analyses being considered particularly robust for determining the sources of ore-forming fluids and S analyses elucidating the sources of ore-forming materials [79,80].

To determine the characteristics and origin of ore-forming fluids, samples of quartz from Stage IV (main ore stage) of the Liziyuan Au deposit were analyzed for H and O isotopes. The δD_{H2O} and calculated $\delta^{18}O_{H2O}$ values of ore fluids in the Liziyuan and other representative Au deposits in the WQOB are shown in Figure 10. The $\delta^{18}O_{H2O}$ values were obtained by calculation based on the isotopic fractionation equation for quartz–H_2O at corresponding temperatures [81,82]. The values for most samples are close to the range of typical magmatic hydrothermal fluid, especially in the Suishizi section, and some of the values from the orogenic gold deposits in the WQOB plot in the magmatic hydrothermal-fluid field, indicating a magmatic-fluid affinity throughout the orogenic gold deposits in the WQOB. Based on these results and the strong temporospatial coupling of Au mineralization and magmatic activity in the late Triassic, we suggest that magmatic fluids were a major component of the ore-forming fluids. In the component plot (Figure 10), the results from our samples trend toward the meteoric water line, suggesting that ore-forming fluids contained meteoric water that had evolved owing to exchange with wall rocks.

The S isotopic compositions of pyrite associated with Au mineralization allowed the determination of the sources of S and Au in hydrothermal systems [83]. Although previous studies have suggested that the sources of S in the Liziyuan deposit were related

to metamorphism, as is the case in a number of orogenic Au deposits worldwide [73], the source of S in the deposit has not yet been well constrained. The samples of pyrite from the three sections of the deposit that were used for S isotope analyses were from either PI or PII mineralization; pyrites from the PI mineralization were separated from banded quartz ores, and pyrites from PII mineralization were extracted from Au-bearing diorite porphyrite and quartz veins. The ranges of δ^{34}S values obtained by the two analytical methods (i.e., sample and in situ analyses) were consistent (Figure 11). The narrow range of positive δ^{34}S values (7.04‰–9.12‰, average 7.65‰) of euhedral–subhedral pyrite from the Au-bearing diorite porphyrite and quartz veins of the Suishizi and Jiancaowan sections, respectively, were consistent with the values for regional quartz diorite (3.8‰ to 13.8‰ [84]), indicating that the S was sourced from oxidized magmatic fluids. The δ^{34}S values of subhedral–anhedral pyrites from the Shenjiagou section (−4.95‰ to −2.44‰) were consistent with those of regional metamorphic strata (−6.6‰ to −2.1‰, Mao, 2001), indicating that the S there was sourced from reduced metamorphic fluids. A further group of δ^{34}S values for quartz-vein euhedral–subhedral pyrites from the Jiancaowan section ranged from 0.10‰ to 3.08‰, indicating a mixed source comprising metamorphic country rocks and magmatic dikes.
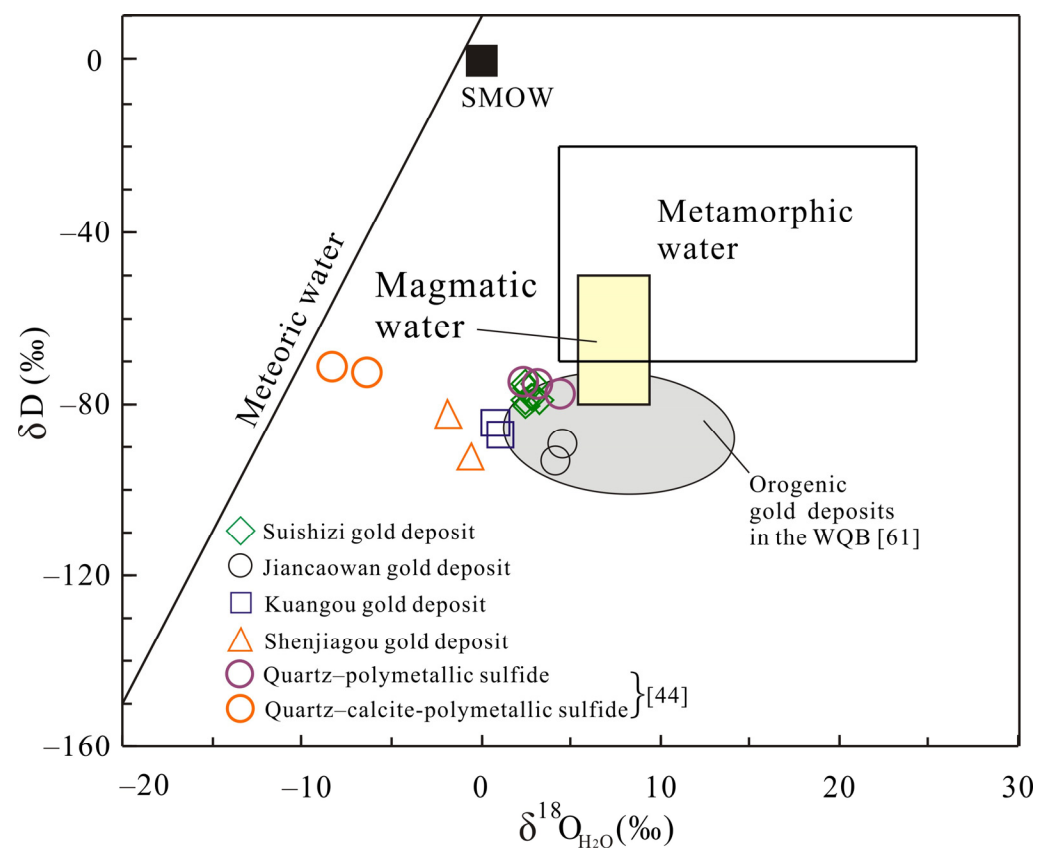
Figure 10. δD and δ^{18}O values of hydrothermal fluids from the Liziyuan Au deposit.

The H–O–S isotopic compositions indicate that ore-forming fluids have magmatic and metamorphic fluid affinities, and a comparison of the δ^{34}S values with those of regional coeval dikes and metamorphic strata indicates that the ore-forming materials included such fluids. This constrains the two-stage mineralization of the Liziyuan Au deposit to earlier metamorphic and later magmatic hydrothermal mineralization. Although the δ^{34}S values of the magmatic hydrothermal mineralization stage (7.04‰–9.12‰) deviated from standard magmatic S compositions (δ^{34}S = 0‰ ± 5‰), they were similar to the values of the magmatic hydrothermal Au deposit in the Jiaodong Au metallogenic belt [85,86], possibly indicating that asthenospheic upwelling triggered the release of gold and sulfur from enriched fertili lithospheric mantle [19,86], as supported by Pb isotopic data for such

interactions published previously [87]. Therefore, we infer that the ore-forming materials during the second stage of the evolution of the Liziyuan Au deposit were derived mainly from the evolution of deep magma.
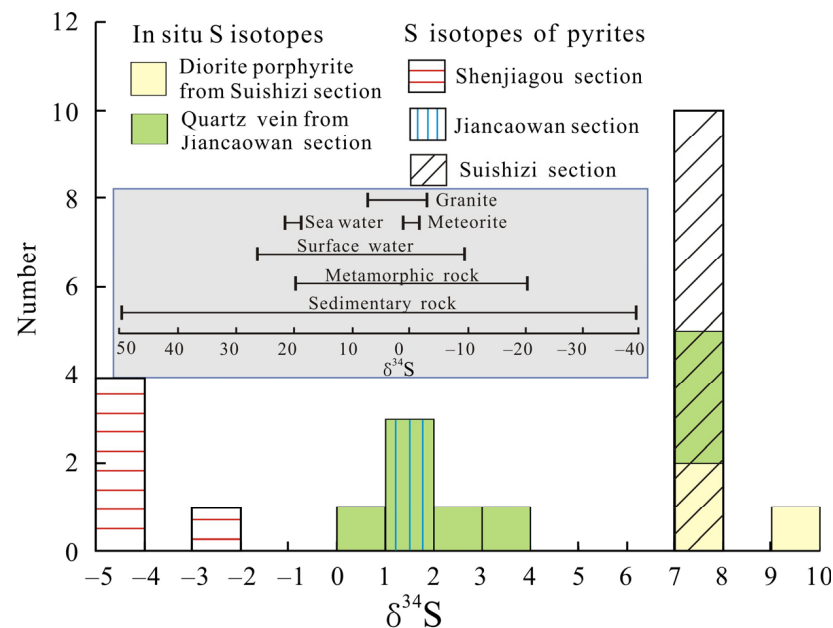

Figure 11. $\delta^{34}S$ values of hydrothermal fluids in the Liziyuan Au deposit.

7.3. Ore Genesis and Metallogenic Dynamics

Most Au deposits are classified as orogenic, Carlin, or Carlin-like in the WQOB, except for minor skarn-type deposits [27,29,88,89]. For the orogenic deposits (including the Liziyuan deposit), previous studies have assumed that, although some deposits coexisted with intermediate–acid magmatic rocks, mineralization was not associated with magmatism [88]. Based on the similarities of its characteristics with those of typical orogenic deposits in terms of ore-controlling structures, ore types, Au occurrence, alteration, and ore-forming fluids, the Liziyuan Au deposit has been classified as an orogenic deposit [73]. Our observations are broadly consistent with this classification, although we suggest that magmatism may have made a substantial contribution to the mineralization.

Previous studies have considered two modes of magmatic activity throughout the WQOB during Paleo-Tethyan evolution, involving (1) magmatic activity caused by northward subduction at 250–237 Ma, syn-collisional events at 237–210 Ma, and a post-collisional setting at 210–185 Ma [45,90–94], and (2) subduction-related magmatism at 245–218 Ma, syn-collisional magmatism at 220–210 Ma, and post-collisional magmatism at 210–200 Ma [34,45]. Uncertainty thus remains with regard to the timing of subduction and syn-collisional magmatism in the WQOB, although a post-collisional stage after 210 Ma is commonly accepted. The Tianzishan monzogranite was formed at 241–236 Ma [62,73]), with the earliest ore-forming period of the Liziyuan Au deposit being dated at 220 Ma. Although isotopic data indicate no direct relationship, the Tianzishan magmatism likely provided a small amount of fluid and thermal power for Au activation and migration, based on the similar mineral assemblages and temporospatial relationship between the Tianzishan monzogranite and the PI mineralization. Therefore, the genesis of the Tianzishan monzogranite may reflect the metallogenic dynamics of the earliest ore-forming stage of the Liziyuan Au deposit. The Tianzishan monzogranite belongs to a high-K calc-alkaline and shoshonitic series characterized by low Y and Yb contents and high Sr/Y (13.3–180.7) and $(La/Yb)_N$ (13.8–48.4) ratios, with most of the Tianzishan monzogranite samples plotting in the adakitic fields in (Sr/Y)–Y and $(La/Yb)_N$–Yb_N diagrams (Figure 12).
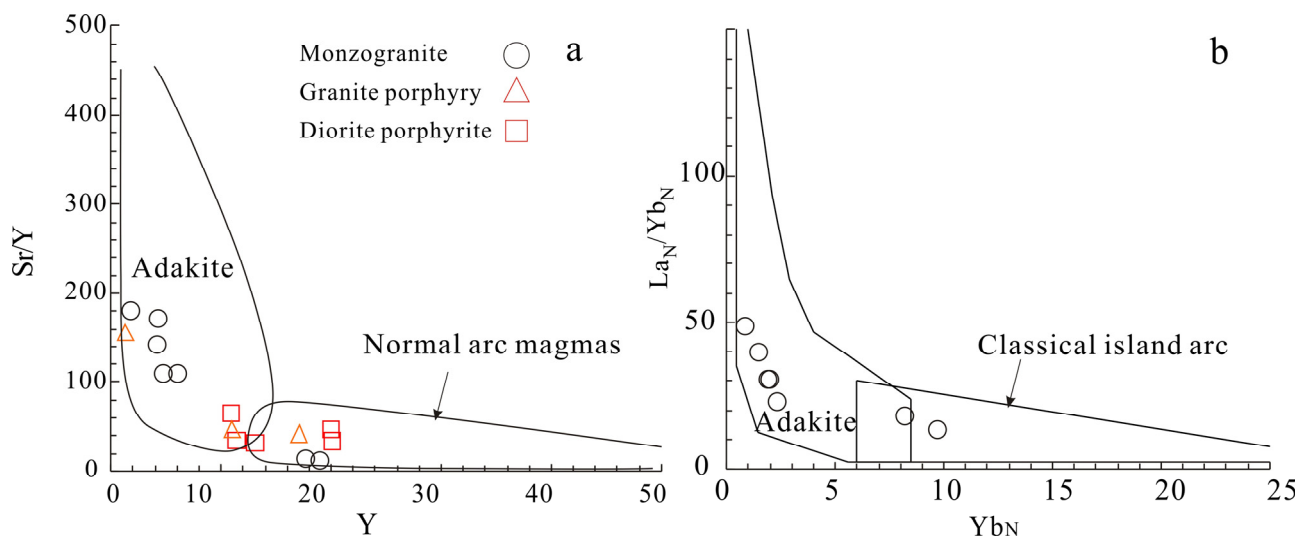
Figure 12. (Sr/Y)–Y (**a**) and (La/Yb)$_N$–Yb$_N$ (**b**) diagrams for the Tianzishan monzogranite, granite porphyry, and diorite porphyrite dike samples (after Defant and Drummond, 1990 [95]).

The geochemical signatures of adakites indicate that they are derived from garnet amphibolite or amphibole sources at depths of >40 km [96,97], with several possible mechanisms for adakitic magma generation having been considered. Assimilation–fractionation–crystallization (AFC) from a basalt source is unlikely for the Tianzishan monzogranite. If the Tianzishan monzogranite exposed over 130 km^2 [74] were the products of an AFC process, an abundance of basaltic rocks would be present in the study area; however, no such lithologies have been identified to date. The Tianzishan monzogranite is enriched in SiO$_2$, K and depleted in Na, with K$_2$O/Na$_2$O ratios of 1.01–1.71, corresponding to high-silica adakitic magma derived from the lower crust metasomatized by subduction fluids [98–102]. Therefore, partial melting of subducted oceanic crust seems an unlikely magma source. Furthermore, in the R1–R2 and Rb–(Y + Ta) tectonic discrimination diagrams (Figure 13), the samples generally plot within the syn-collision field, near the junction with the volcanic arc field, implying that they were generated in a collisional setting. Derivation of the Tianzishan monzogranite from partial melting of thickened lower crust is thus a more likely model. The monzogranite samples are enriched in LREEs, Rb, Th, U, and Pb and depleted in Nb, P, and Ti, consistent with the elemental composition of the crust [103]. Their depletion in Na, Ta, and HREEs, with flat HREE patterns, indicates that residual facies in the magmatic source were mainly garnet facies [95]. We conclude that the Tianzishan monzogranite was derived from partial melting of thickened lower crust. The Tianzishan monzogranite was exposed as oval outcrops with the principal axes of stress lying parallel to the Mianlue suture, indicating an extrusive environment during formation. Based on previously published ore and fluid characteristics [73], we consider that the Tianzishan monzogranite and the Liziyuan Au deposit (PI) formed in response to orogenesis.

Dating of magmatic rocks and magmatic hydrothermal fluids related to the later mineralization period of the Liziyuan Au deposit yielded ages of 213–199 Ma. Most of the granite porphyry and diorite porphyrite samples had lower Sr/Y (33.7–66.1) ratios than those of the Tianzishan monzogranite, implying they were formed in a different tectonic setting. In the tectonic discrimination diagram (Figure 13b), the samples plot in or near the post-collisional field. Our dating results (213–199 Ma) and the occurrence of later magmatic–hydrothermal mineralization in a post-collisional setting were consistent with the tectonic settings described in previous studies [34,45,93,94,104]. The later magmatic hydrothermal mineralization of the Liziyuan Au deposit thus occurred in a post-collisional extensional setting. To summarize, the Liziyuan Au deposit is an orogenic deposit that underwent early collisional compression and mineralization owing

to metamorphic fluids, with later post-collisional–extensional magmatic–hydrothermal superimposition (Figure 14).
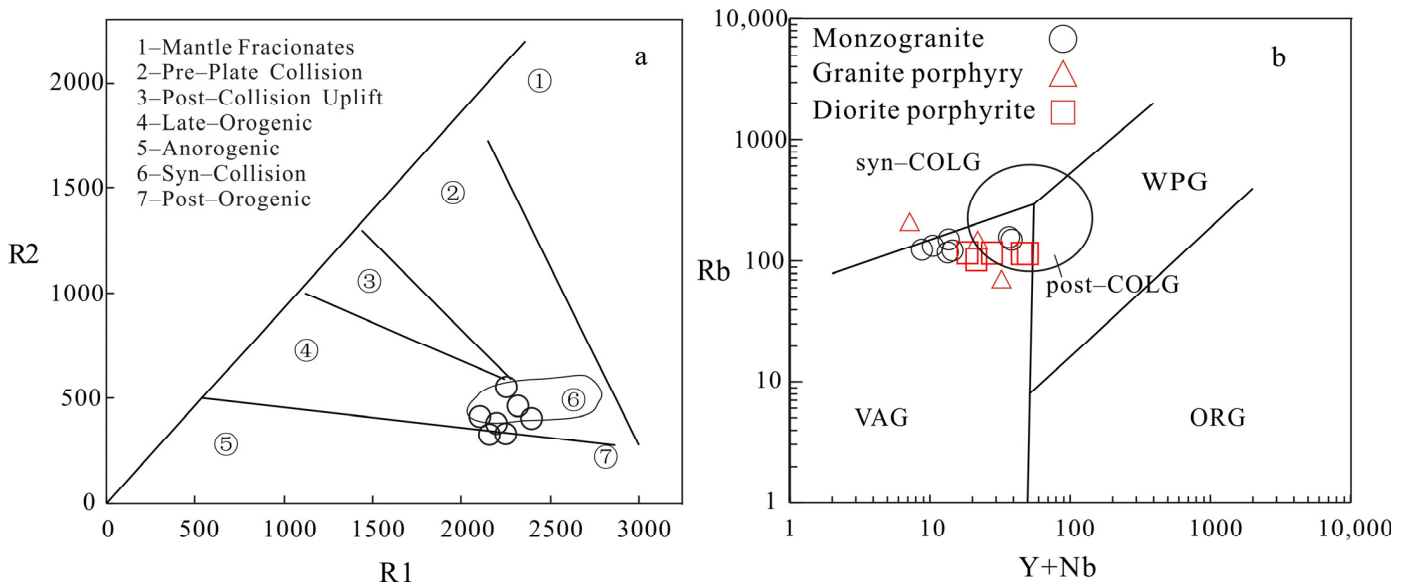
Figure 13. R1–R2 (**a**) and Rb–(Y + Nb) (**b**) diagrams for the Tianzishan monzogranite, granite porphyry and diorite porhpyrite dike samples.
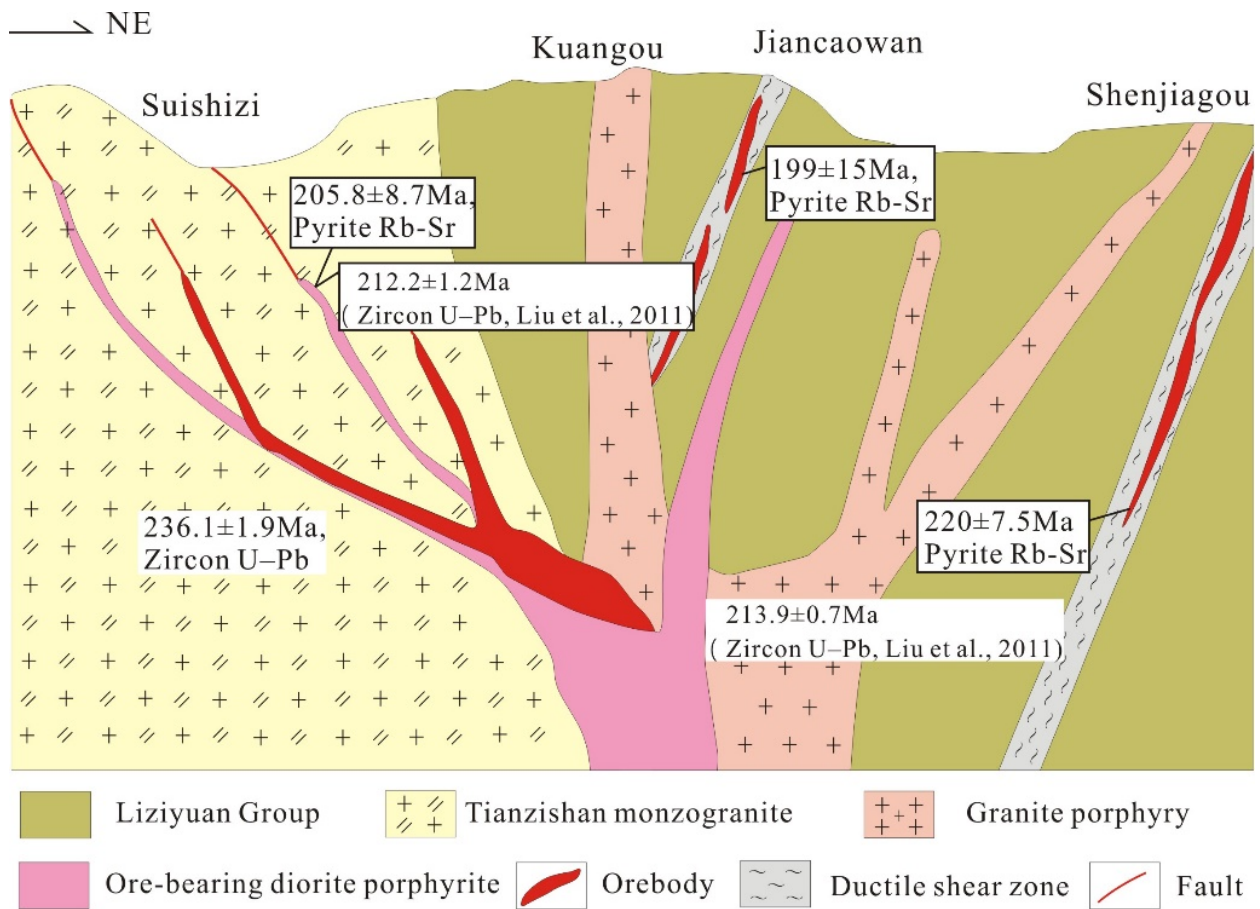

Figure 14. Metallogenic model of Liziyuan Au deposit.

8. Conclusions

The Liziyuan Au deposit is a typical orogenic Au deposit in the WQOB. Geochronological data indicate two periods of intrusive magmatism (236.1 and 213.9–212.2 Ma) related to the orebodies, predating two Au mineralization periods (220.5 Ma and 205.8–199 Ma) by 5–10 Myr, which indicates a close temporospatial relationship between the mineralization and magmatism. H–O–S isotopic signatures indicate that ore-forming fluids and materials were exsolved from surrounding metasedimentary volcanic rocks and dioritic porphyrite and granite porphyry dikes, with the Au endowment of the deposit being associated with several Au mineralization events and multiple metamorphic and magmatic hydrothermal episodes. The results of this study suggest that the Liziyuan orogenic Au deposit was the product of superimposed mineralization involving earlier collisional–compressional metamorphism and later post-collisional–extensional magmatic fluids related to the evolution of the WQOB.

References

1. Groves, D.I. The crustal continuummodel for late Archean lode gold deposits of the Yilgarn block, western Australia. *Miner. Depos.* **1993**, *28*, 366–374. [CrossRef]
2. Groves, D.I.; Goldfarb, R.J.; Gebre-Mariam, M.; Hagemann, S.G.; Robert, F. Orogenic gold deposits: A proposed classification in the context of their crustal distribution and relationship to other gold deposit types. *Ore Geol. Rev.* **1998**, *13*, 7–27. [CrossRef]
3. Goldfarb, R.J.; Baker, T.; Dubé, B.; Groves, D.I.; Hart, C.J.; Gosselin, P. Distribution, Character, and Genesis of Gold Deposits in Metamorphic Terran. *One Hundredth Anniv. Vol.* **2005**, 407–450. [CrossRef]
4. Kolb, J.; Dziggel, A.; Bagas, L. Hypozonal lode gold deposits: A genetic concept based on a review of the New Consort, Renco, Hutti, Hira Buddini, Navachab, Nevoria and the Granites deposits. *Precambrian Res.* **2015**, *262*, 20–44. [CrossRef]
5. Frimmel, H.E. Episodic concentration of gold and ore grade through Earth's history. *Earth Sci. Rev.* **2018**, *180*, 148–158. [CrossRef]
6. Groves, D.I.; Santosh, M. Craton and thick lithosphere margins: The sites of giant mineral deposits and mineral provinces. *Gondwana Res.* **2020**, *100*, 195–222. [CrossRef]
7. Groves, D.I.; Santosh, M.; Deng, J.; Wang, Q.; Yang, L.; Zhang, L. A holistic model for the orogenic gold deposits and its implication for exploration. *Mineral. Depos.* **2020**, *55*, 275–292. [CrossRef]
8. Beaudoin, G.; Pitre, D. Stable isotope geochemistry of the Archean Val-d 'Or (Canada) orogenic gold vein field. Mineral. *Deposita* **2005**, *40*, 59–75. [CrossRef]
9. Phillips, G.; Powell, R. Formation of gold deposits: A metamorphic devolatilzation model. *J. Metamorph. Geol.* **2010**, *28*, 689–718. [CrossRef]
10. Wyman, D.A.; Cassidy, K.F.; Hollings, P. Orogenic gold and the mineral systems approach: Resolving fact, fiction and fantasy. *Ore Geol. Rev.* **2016**, *78*, 322–335. [CrossRef]
11. Chinnasamy, S.S.; Mishra, B. Greenstone metamorphism, hydrothermal alteration, and gold mineralization in the genetic context of the granodiorite-hosted gold deposit at Jonnagiri, Eastern Dharwar Craton. India. *Econ. Geol.* **2013**, *108*, 1015–1036. [CrossRef]
12. Pitcairn, I.K.; Craw, D.; Teagle, D.A. Metabasalts as sources of metals in orogenic gold deposits. *Mineral. Depos.* **2015**, *50*, 373–390. [CrossRef]

13. Lawley, C.J.M.; Creaser, R.A.; Jackson, S.E.; Yang, Z.; Davis, B.J.; Pehrsson, S.J.; Dube, B.; Mercier-Langevin, P.; Vaillancourt, D. Unraveling the Western Churchill Province paleoproterozoic gold metallotect: Constraints from Re-Os arsenopyrite and U-Pb xenotime geochronology and LA-ICP-MS arsenopyrite trace element chemistry at the BIF-hosted Meliadine Gold District, Nunavut, Canada Economic. *Geology* **2015**, *110*, 1425–1454.

14. Cave, B.J.; Pitcairn, I.K.; Craw, D.; Large, R.R.; Thompson, J.M.; Johnson, S.C. A metamorphic mineral source for tungsten in the turbidite-hosted orogenic gold deposits of the Otago Schist, New Zealand. *Miner. Depos.* **2017**, *52*, 515–537. [CrossRef]

15. Wu, Y.-F.; Li, J.-W.; Evans, K.; Koenig, A.E.; Li, Z.-K.; O'Brien, H.; Lahaye, Y.; Rempel, K.; Hu, S.-Y.; Zhang, Z.-P. Ore-forming processes of the Daqiao Epizonal Orogenic gold deposit, West Qinling Orogen, China: Constraints from textures, trace elements, and sulfur isotopes of pyrite and marcasite, and Raman spectroscopy of carbonaceous material. *Econ. Geol.* **2018**, *113*, 1093–1132. [CrossRef]

16. Patten, C.; Pitcairn, I.; Molnar, F.; Kolb, J.; Beaudoin, G.; Guilmette, C.; Peillod, A. Gold mobilization during metamorphic devolatilization of Archean and Paleoproterozoic metavolcanic rocks. *Geology* **2020**, *48*, 1110–1114. [CrossRef]

17. Goldfarb, R.J.; Groves, D.I. Orogenic gold: Common or evolving fluid and metal sources through time. *Lithos* **2015**, *233*, 2–26. [CrossRef]

18. Phillips, G.N.; Groves, D.I. The nature of Archaean gold-bearing fluids as deduced from gold deposits of Western Australia. *J. Geol. Soc. Aust.* **1983**, *30*, 25–39. [CrossRef]

19. Deng, J.; Wang, Q.; Santosh, M.; Liu, X.; Liang, Y.; Yang, L.; Zhao, R.; Yang, L. Remobilization of metasomatized mantle lithosphere: A new model for the Jiaodong gold province, eastern China. *Miner. Depos.* **2020**, *55*, 257–274. [CrossRef]

20. Wang, C.; Shao, Y.J.; Evans, N.J.; Li, H.; Zhou, H.D.; Huang, K.X.; Liu, Z.F.; Chen, Y.; Lai, C.; Liu, Q.Q. Genesis of Zixi gold deposit in Xuefengshan, Jiangnan Orogen (South China): Age, geology and isotopic constraints. *Ore Geol. Rev.* **2020**, *117*, 103301. [CrossRef]

21. Wang, Q.; Zhao, H.; Groves, D.I.; Deng, J.; Zhang, Q.; Xue, S. The Jurassic Danba hypozonal orogenic gold deposit, western China: Indirect derivation from fertile mantle lithosphere metasomatized during Neoproterozoic subduction. *Miner. Depos.* **2020**, *55*, 309–324. [CrossRef]

22. Burrows, D.R.; Wood, P.C.; Spooner, E.T.C. Carbon isotope evidence for a magmatic origin for Archean gold-quartz vein ore deposits. *Nature* **1986**, *321*, 851–854. [CrossRef]

23. Xue, Y.; Campbell, I.; Ireland, T.R.; Holden, P.; Armstrong, R. No mass-independent sulfur isotope fractionation in auriferous fluids supports a magmatic origin for Archean gold deposits. *Geology* **2013**, *41*, 791–794. [CrossRef]

24. Bath, A.B.; Walshe, J.L.; Cloutier, J.; Verrall, M.; Cleverley, J.S.; Pownceby, M.I.; Macrae, C.M.; Wilson, N.C.; Tunjic, J.; Nortje, G.S. Biotite and Apatite as Tools for Tracking Pathways of Oxidized Fluids in the Archean East Repulse Gold Deposit, Australia. *Econ. Geol.* **2013**, *108*, 667–690. [CrossRef]

25. Lawrence, D.M.; Treloar, P.J.; Rankin, A.H.; Harbidge, P.; Holliday, J. The geology and mineralogy of the Loulo Mining District, Mali, West Africa: Evidence for two distinct styles of orogenic gold mineralization. *Econ. Geol.* **2013**, *108*, 199–227. [CrossRef]

26. Spence-Jones, C.P.; Jenkin, G.R.T.; Boyce, A.J.; Hill, N.J.; Sangster, C.J.S. Tellurium, magmatic fluids and orogenic gold: An early magmatic fluid pulse at Cononish gold deposit, Scotland. *Ore Geol. Rev.* **2018**, *102*, 894–905. [CrossRef]

27. Mao, J.; Qiu, Y.; Richard; Goldfarb, R.J.; Zhang, Z.; Steve; Garwin, S.; Fengshou, R. Geology, distribution, and classification of gold deposits in the western Qinling belt, central China. *Mineral. Deposita* **2002**, *37*, 352–377. [CrossRef]

28. Zhou, T.; Goldfarb, R.J.; Phillips, N.G. Tectonics and distribution of gold deposits in China-an overview. *Miner. Depos.* **2002**, *37*, 249–282. [CrossRef]

29. Chen, Y.J.; Santosh, M. Triassic tectonics and mineral systems in the Qinling Orogen, central China. *Geol. J.* **2014**, *4*, 338–358. [CrossRef]

30. Goldfarb, R.J.; Taylor, R.D.; Collins, G.S.; Goryachev, N.A.; Orlandini, O.F. Phanerozoic continental growth and gold metallogeny of Asia. *Gondwana Res.* **2014**, *25*, 48–102. [CrossRef]

31. Deng, J.; Wang, Q.F. Gold mineralization in China: Metallogenic provinces, deposit types and tectonic framework. *Gondwana Res.* **2016**, *36*, 219–274. [CrossRef]

32. Meng, Q.R.; Zhang, G.W. Geologic framework and tectonic evolution of the Qinling orogen, central China. *Tectonophysics* **2000**, *323*, 183–196. [CrossRef]

33. Ratschbacher, L.; Hacker, B.R.; Calvert, A.; Webb, L.E.; Grimmer, J.C.; McWilliams, M.O.; Ireland, T.; Dong, S.W.; Hu, J.M. Tectonics of the Qinling (Central China): Tectonostratigraphy, geochronology, and deformation history. *Tectonophysics* **2003**, *366*, 1–53. [CrossRef]

34. Dong, Y.P.; Santosh, M. Tectonic architecture and multiple orogeny of the Qinling Orogenic Belt, Central China. *Gondwana Res.* **2016**, *29*, 1–40. [CrossRef]

35. Dong, Y.P.; Yang, Z.; Liu, X.; Sun, S.; Li, W.; Cheng, B.; Zhang, F.; Zhang, X.; He, D.; Zhang, G. Mesozoic intracontinental orogeny in the Qinling Mountains, central China. *Gondwana Res.* **2016**, *30*, 144–158. [CrossRef]

36. Tang, L.; Santosh, M.; Dong, Y.; Tsunogae, T.; Zhang, S.; Cao, H. Early Paleozoic tectonic evolution of the North Qinling orogenic belt: Evidence from geochemistry, phase equilibrium modeling and geochronology of metamorphosed mafic rocks from the Songshugou ophiolite. *Gondwana Res.* **2016**, *30*, 48–64. [CrossRef]

37. Li, S.Z.; Zhao, S.J.; Liu, X.; Cao, H.H.; Yu, S.; Li, X.Y.; Somerville, I.; Yu, S.Y.; Suo, Y.H. Closure of the Proto-Tethys Ocean and Early Paleozoic amalgamation of microcontinental blocks in East Asia. *Earth Sci. Rev.* **2018**, *186*, 37–75. [CrossRef]

38. Yan, Q.R.; Wang, Z.Q.; Hanson, A.D.; Druschke, P.A.; Yan, Z.; Liu, D.Y.; Jian, P.; Song, B.; Wang, T.; Jiang, C.F. SHRIMP age and geochemistry of the Bikou volcanic terrane: Implications for Neoproterozoic tectonics on the northern margin of the Yangtze craton. *Acta Geol. Sin. (Engl. Ed.)* **2003**, *77*, 479–490.

39. Deng, J.; Wang, Q.F.; Li, G.J.; Santosh, M. Cenozoic tectono-magmatic and metallogenic processes in the Sanjiang region, southwestern China. *Earth Sci. Rev.* **2014**, *138*, 268–299. [CrossRef]

40. Yu, H.C.; Guo, C.A.; Qiu, K.F.; Duncan, M.; Jiang, G.P.; Gou, Z.Y.; Li, B.L. Geochronological and Geochemical Constraints on the Formation of the Giant Zaozigou Au-Sb Deposit, West Qinling. China. *Minerals* **2019**, *9*, 37. [CrossRef]

41. Wu, Y.F.; Li, J.W.; Evans, K.; Vasconcelos, P.M.; Thiede, D.S.; Fougerouse, D.; Rempel, K. Late Jurassic to early Cretaceous age of the Daqiao gold deposit, West Qinling orogen, China: Implications for regional metallogeny. *Miner. Depos.* **2019**, *54*, 631–644. [CrossRef]

42. Du, Z.T.; Wu, G.G. *Study on Tectonic Systems and Gold Metallogenic Tectonic-Dynamics in the Region of West Qinling*; Geological Publishing House: Beijing, China, 1998; pp. 1–145, (In Chinese with English Abstract).

43. Chen, Y.J.; Pirajno, F.; Sui, Y.H. Isotope geochemistry of the Tieluping silver-lead deposit, Henan, China: A case study of orogenic silver-dominated deposits and related tectonic setting. *Miner. Depos.* **2004**, *39*, 560–575. [CrossRef]

44. Yang, L.Q.; Deng, J.; Dilek, Y.; Qiu, K.F.; Ji, X.Z.; Li, N.; Taylor, R.D.; Yu, J.Y. Structure, geochronology, and petrogenesis of the Late Triassic Puziba granitoid dikes in the Mianlue suture zone, Qinling Orogen. China. *Geol. Soc. Am. Bull.* **2015**, *11*, 1831–1854. [CrossRef]

45. Dong, Y.P.; Zhang, G.W.; Neubauer, F.; Liu, X.M.; Genser, J.; Hauzenberger, C. Tectonic evolution of the Qinling orogen, China: Review and Synthesis. *J. Asian Earth Sci.* **2011**, *41*, 213–237. [CrossRef]

46. Li, L.; Li, S.R.; Santosh, M.; Zhu, J.; Suo, X.J. Early Jurassic decratonic gold metallogenesis in the Eastern North China Craton: Constraints from S-Pb-C-D-O isotopic systematics and pyrite Rb-Sr geochronology of the Guilaizhuang Te-Au deposit. *Ore Geol. Rev.* **2018**, *92*, 558–568. [CrossRef]

47. Qiu, K.F.; Yu, H.C.; Gou, Z.Y.; Liang, Z.L.; Zhang, J.L.; Zhu, R. Nature and origin of Triassic igneous activity in the Western Qinling Orogen: The Wenquan composite pluton example. *Int. Geol. Rev.* **2018**, *60*, 242–266. [CrossRef]

48. Su, C.Q.; Cui, J.J.; Zhao, X.; Li, Y.; Pei, X.Z.; Yang, X.K. Re-definition and its attribute of the Dacaotan Formation in western Qinling. *Coal Geol. Explor.* **2004**, *34*, 1–6.

49. Chen, L.; Yuan, H.L.; Chen, K.Y.; Bao, Z.A.; Zhu, L.M.; Liang, P. In situ sulfur isotope analysis by laser ablation MC-ICPMS and a case study of the Erlihe Zn-Pb ore deposit, Qinling Orogenic Belt, Central China. *J. Asian Earth Sci.* **2019**, *176*, 325–336. [CrossRef]

50. Bendall, C.; Lahaye, Y.; Fiebig, J.; Weyer, S.; Brey, G.P. In situ sulfur isotope analysis by laser ablation MC-ICPMS. *Appl. Geochem.* **2006**, *21*, 782–787. [CrossRef]

51. Mason, P.R.D.; Kosler, J.; de Hoog, J.C.M.; Sylvester, P.J.; Meffan-Main, S. In-situ determination of sulfur isotopes in sulfur-rich materials by laser ablation multiplecollector inductively coupled plasma mass spectrometry, LA-MC-ICP-MS. *J. Anal. At. Spectrom.* **2006**, *21*, 177–186. [CrossRef]

52. Clayton, R.N.; Mayeda, T.K. The use of bromine and pentafluoride in the extraction of oxygen from oxide and silicates for isotopes analyses. *Geochim. Cosmochim. Acta* **1963**, *27*, 43–52. [CrossRef]

53. Coleman, M.L.; Shepherd, T.J.; Durham, J.J.; Rouse, J.E.; Moore, G.R. Reduction of water with zinc for hydrogen isotope analysis. *Anal. Chem.* **1982**, *54*, 993–995. [CrossRef]

54. Zheng, Y.F.; Hoefs, J. Carbon and oxygen isotopic covariations in hydrothermal calcites. *Miner. Depos.* **1993**, *28*, 79–89. [CrossRef]

55. Compston, W.; Williams, I.S.; Mayer, C. U-Pb geochronology of zircons from Lunar Breccia 73217 using a sensitive high resolution ion microprobe: Proc. XIV Lunar Planetary Science Conference. *J. Geophys. Res.* **1984**, *89*, B525–B534. [CrossRef]

56. Compston, W.; Willians, I.S.; Kirsdivink, J.L. Zircon U-Pb ages for the Early Cambrian tine-scale. *J. Geol. Soc. Lond.* **1992**, *149*, 171–184. [CrossRef]

57. Williams, I.S. U-Th-Pb geochronology by ion microprobe. *Rev. Econ. Geol.* **1998**, *7*, 1–35.

58. Ludwig, K.R. Isoplot 3.00: A Geochronological Toolkit for Microsoft Excel. *Berkeley Geochronol. Cent. Spec. Publ.* **2003**, *4*, 70.

59. Chen, D.; Liu, Y.H.; Wang, K.L.; Li, Z.G.; Gao, H.X.; Zhang, J.; Qi, X.S. Superimposed mineralization of gold deposits in Liziyuan district, Western Qinling Mountains. *Gold* **2014**, *8*, 15–21, (In Chinese with English Abstract).

60. Zhang, Y.Z.; Qu, H.L.; Cheng, S.L. Discussion on the metallogenic model of the Li Zi Yuan gold deposit in Western Qinling Mountains. *Miner. Resour.* **2018**, *11*, 121–122, (In Chinese with English Abstract).

61. Liu, J.J.; Liu, C.H.; Carranza, E.J.M.; Li, Y.J.; Mao, Z.H.; Wang, J.P.; Wang, Y.H.; Zhang, J.; Zhai, D.G.; Zhang, H.F.; et al. Geological characteristics and ore-forming process of the gold deposits in the western Qinling region. China. *J. Asian Earth Sci.* **2015**, *103*, 40–69. [CrossRef]

62. He, G.C.; Li, J.W.; Zu, B.; Liu, W.J.; Qiu, H.N.; Bai, X.J. Sericite 40Ar/39Ar and zircon U-Pb dating of the Liziyuan gold deposit, West Qinling orogen, central China: Implications for ore genesis and tectonic setting. *Ore Geol. Rev.* **2021**, *139*, 104531. [CrossRef]

63. Yu, H.C.; Qiu, K.F.; Sai, S.X.; McIntire, D.C.; Pirajno, F.; Duo, D.W.; Miggins, D.P.; Wang, J.; Jia, R.Y.; Wu, M.Q. Paleo-tethys late triassic orogenic gold mineralization recorded by the Yidi' nan gold deposit, West Qinling, China. *Ore Geol. Reviess* **2020**, *116*, 103211. [CrossRef]

64. Aibai, A.; Deng, X.H.; Pirajno, R.; Han, S.; Liu, W.X.; Li, X.; Chen, X.; Wu, Y.S.; Bao, Z.L.; Chen, Y.J. Geology and geochronology of the Tokuzbay gold deposit in the Chinese Altai: A case study of collision-related orogenic gold deposits in Central Asian Orogenic Belt. *Ore Geol. Rev.* **2021**, *136*, 104261. [CrossRef]

65. Du, B.S.; Shen, J.F.; Santosh, M.; Liu, H.M.; Liu, J.J.; Wang, S.H.; Xu, K.X. Genesis of the Gangcha gold deposit, West Qinling Orogen, China: Constraints from Rb-Sr geochronology, in-situ sulfur isotopes and trace element geochemistry of pyrite. *Ore Geol. Riviews* **2021**, *138*, 104350. [CrossRef]

66. Li, Z.H.; Li, B.L.; Chen, S.L.; Li, P.; Liao, Y.B.; Yu, R.T. Geochronology, Geochemistry, Hfisotope, and their geological significance of the tonalite and fine-grained diorite from Kushuiquan gold deposit, North Qaidam. *Acta Petrol. Sin.* **2021**, *37*, 1653–1673. (In Chinese with English Abstract)

67. Ma, J.; Lü, X.; Li, S.; Chen, J.; Lu, F.; Yin, X.; Wu, M. The ca. 230 Ma gold mineralization in the Fengtai Basin, Western Qinling orogen, and its implications for ore genesis and geodynamic setting: A case study of the Matigou gold deposit. *Ore Geol. Rev.* **2021**, *138*, 104398. [CrossRef]

68. Li, Q.L.; Chen, F.K.; Yang, J.H.; Fan, H.R. Single grain pyrite Rb-Sr dating of the Linglong gold deposit, eastern China. *Ore Geol. Rev.* **2008**, *34*, 263–270. [CrossRef]

69. Henjes, K.F.; Prochaska, W.; Niedermayr, A.; Sullivan, N.; Baxter, E. Sm-Nd dating of hydrothermal carbonate formation: An example from the Breitenau magnesite deposit (Styria, Austria). *Chem. Geol.* **2014**, *387*, 184–201. [CrossRef]

70. Zeng, Y.J.; Li, L.; Li, S.R.; Santosh, M.; Song, Y.X.; Alam, M. Rb-Sr geochronology and geochemistry of pyrite from the Shihu gold deposit, central North China Craton: Implication for the timing and genesis of gold mineralization. *Geol. J.* **2019**, *55*, 5779–5790. [CrossRef]

71. Nakai, S.I.; Halliday, A.N.; Kesler, S.E.; Jones, H.D. Rb-Sr dating of sphalerites from Tennessee and the genesis of Mississippi Valley type ore deposits. *Nature* **1990**, *346*, 354–357. [CrossRef]

72. Pettke, T.; Dianmond, W. Rb-Sr dating of sphalerite based on fluid inclusion-host mineral isochrons: A clarification of why it works. *Econ. Geol.* **1996**, *91*, 951–956. [CrossRef]

73. Yang, T.; Zhu, L.M.; Zhang, G.W.; Wang, F.; Lu, R.K.; Xia, J.C.; Zhang, Y.Q. Geological and geochemical constraints on genesis of the Liziyuan gold-dominated polymetal deposit, western Qinling orogen, central China. *Int. Geol. Rev.* **2012**, *54*, 1944–1966. [CrossRef]

74. Lv, Y.B. Characteristics and Genesis of the Tianzishan Plution in the Liziyuan-Taiyangse Area, Gansu Province. Master's Thesis, China University of Geosciences, Wuhan, China, 2019. (In Chinese with English Abstract)

75. Liu, Y.H.; Liu, H.L.; Huang, S.F.; Gao, H.X.; Zhang, Y.Q.; Li, Z.G.; Zheng, X.Z. Metallogenic epoch and geological features of Suishizi porphyry gold deposit in Liziyuan area, west Qinling mountain. *Gold* **2011**, *32*, 12–18, (In Chinese with English Abstract).

76. Li, W.B.; Huang, Z.L.; Xu, D.R.; Chen, J.; Xu, C.; Guan, T. Rb-Sr isotopic method on zinc-lead ore deposits: A review. *Geotecton. Metallog.* **2002**, *26*, 436–441. (In Chinese with English Abstract)

77. Wang, S.; Sun, F.Y.; Wang, G.; Liu, K.; Li, L.; Guo, H.L. Phanerozoic magmatic evolution and metallogenesis in the Eastern Jilin and Heilongjiang Provinces, China. *Int. Geol. Rev.* **2019**, *61*, 2227–2248. [CrossRef]

78. Tan, J.; Wei, J.H.; Tan, W.J.; Guo, D.Z. Statistic study of diagenesis-mineralization time gap for comagmatic gold deposits. *Geol. Rev.* **2006**, *52*, 54–62.

79. Ohmoto, H.; Rye, R.O. Isotopes of sulfur and carbon. In *Geochemistry of Hydrothermal Ore Deposits*; Barnes, H.L., Ed.; Wiley: New York, NY, USA, 1979; pp. 509–567.

80. Taylor, H.P. Oxygen and hydrogen isotope relationships in hydrothermal mineral deposits. In *Geochemistry of Hydrothermal Ore Deposits 3*; Barnes, H.L., Ed.; Wiley: New York, NY, USA, 1997; pp. 229–302.

81. O' Neil, J.R.; Clayton, R.N.; Mayeda, T.K. Oxygen isotope fractionation in divalent metal carbonates. *J. Chem. Phys.* **1969**, *51*, 5547–5558. [CrossRef]

82. Clayton, R.N.; O' Neil, J.R.; Mayeda, T.K. Oxygen isotope exchange between quartz and water. *J. Geophys. Res. Atmos.* **1972**, *77*, 3057–3067. [CrossRef]

83. Kesler, S.E.; Riciputi, L.C.; Ye, Z. Evidence for amagmatic origin for Carlin-type gold deposits: Isotopic composition of sulfur in the betze-post-screamer deposit, Nevada, USA. *Miner. Depos.* **2005**, *40*, 127–136. [CrossRef]

84. Mao, J.W. Geology, distribution and classification of gold deposit in the Western Qinling Belt, central China. *Bull. Mineral. Petrol. Geochem.* **2001**, *20*, 11–13. [CrossRef]

85. Wang, Z.L. Metallogenic System of Jiaojia Gold Orefield, Shandong Province, China. Ph.D. Thesis, China University of Geosciences, Wuhan, China, 2012. (In Chinese with English Abstract)

86. Zhang, Z.R.; Wang, Z.L.; Wang, S.R.; Liu, Y.; Qin, K.W. Metallognic mechanism of Dayingezhuang gold deposit, northwestern Jiaodong Peninsula: Geochemistry constrains from the gold bearing pyrite typomorph and sulfur isotope. *Acta Petrol. Sin.* **2016**, *32*, 2451–2464. (In Chinese with English Abstract)

87. Wei, J.Q. Geological Features and Metallogenic Regularity of Suishizi Gold Deposit in Liziyuan, Tianshui. Master's Thesis, Chang'an University, Xi'an, China, 2011. (In Chinese with English Abstract)

88. Liu, J.J.; Liu, C.H.; Wang, J.P.; Zhu, L.M.; Zhang, J.; Zhai, D.G.; Wang, Y.H.; Liu, Z.J.; Zhang, F.F. Classification and mineralization of the gold deposits in the western Qinling region. China. *Earth Sci. Front.* **2019**, *26*, 1–16, (In Chinese with English Abstract).

89. Qiu, K.F.; Yu, H.C.; Deng, J.; McIntire, D.; Gou, Z.-Y.; Geng, J.Z.; Chang, Z.S.; Zhu, R.; Li, K.N.; Goldfarb, R. The giant Zaozigou Au-Sb deposit in West Qinling, China: Magmatic- or metamorphic-hydrothermal origin? *Miner. Depos.* **2020**, *55*, 345–362. [CrossRef]

90. Mattauer, M.; Matte, P.; Malavieille, J.; Tapponnier, P.; Maluski, H.; Xu, Z.Q.; Lu, Y.L.; Tang, Y.Q. Tectonics of the Qinling Belt: Build-up and evolution of eastern Asia. *Nature* **1985**, *317*, 496–500. [CrossRef]

91. Luo, B.J.; Zhang, H.F.; Xu, W.C.; Guo, L.; Pan, F.B.; Yang, H. The Middle Triassic Meiwu batholith, West Qinling, central China: Implications for the evolution of compositional diversity in a composite batholith. *J. Petrol.* **2015**, *56*, 1139–1172. [CrossRef]

92. Li, N.; Chen, Y.J.; Santosh, M.; Pirajno, F. Compositional polarity of Triassic granitoids in the Qinling Orogen, China: Implication for termination of the northernmost paleo-Tethys. *Gondwana Res.* **2015**, *27*, 244–257. [CrossRef]

93. Jin, X.Y.; Li, J.W.; Hofstra, A.H.; Sui, J.X. Magmatic-hydrothermal origin of the early Triassic Laodou lode gold deposit in the Xiahe-Hezuo district, West Qinling orogen, China: Implications for gold metallogeny. *Miner. Depos.* **2017**, *52*, 883–902. [CrossRef]

94. Sui, J.X.; Li, J.W.; Jin, X.Y.; Vasconcelos, P.; Zhu, R. 40Ar/39Ar and U-Pb constraints on the age of the Zaozigou gold deposit, Xiahe-Hezuo district, West Qinling orogen, China: Relation to early Triassic reduced intrusions emplaced during slab rollback. *Ore Geol. Rev.* **2018**, *101*, 885–899. [CrossRef]

95. Defant, M.J.; Drummond, M.S. Derivation of some modern arc magmas by melting of young subducted lithosphere. *Nature* **1990**, *34*, 662–665. [CrossRef]

96. Sen, C.; Dunnt, T. Dehydration melting of a basaltic composition amphibolite at 1.5 and 2.0 Gpa: Implication for the origin of adakites. *Contrib. Mineral. Petrol.* **1994**, *117*, 394–409. [CrossRef]

97. Rapp, P.R.; Shimizu, N.; Norman, M.D.; Applegate, G.S. Reaction between slab-derived melt and peridotite in the mantle wedge: Experimental constrains at 3.8 Gpa. *Chem. Geol.* **1999**, *160*, 335–356. [CrossRef]

98. Rapp, R.P.; Xiao, L.; Shimizu, N. Experimental constraints on the origin of potassium-rich adakites in eastern China. *Acta Petrol. Sin.* **2002**, *18*, 193–302.

99. Zhang, Q. Reappraisal of the origin of C-type adakitic rocks from East China. *Acta Petrol. Mineral.* **2011**, *30*, 739–747. (In Chinese with English Abstract)

100. Moyen, J.F. High Sr/Y and La/Yb ratios: The meaning of the "adakitic signature". *Lithos* **2009**, *112*, 556–574. [CrossRef]

101. Yousefi, F.; Sadeghian, M.; Wanhainen, C.; Ghasemi, H.; Frei, D. Geochemistry, petrogenesis and tectonic setting of middle Eocene hypabyssal rocks of the Torud–Ahmad Abad magmatic belt: An implication for evolution of the northern branch of Neo-Tethys Ocean in Iran. *J. Geochem. Explor.* **2017**, *178*, 1–15. [CrossRef]

102. Yousefi, F.; Sadeghian, M.; Lentz, D.R.; Wanhainen, C.; Mills, R.D. Petrology, petrogenesis, and geochronology review of the Cenozoic adakitic rocks of northeast Iran: Implications for evolution of the northern branch of Neo-Tethys. *Geol. J.* **2021**, *56*, 298–315. [CrossRef]

103. Hofmann, A.W. Mantle geochemistry: The message from oceanic volcanism. *Nature* **1997**, *385*, 219–229. [CrossRef]

104. Li, R.; Pei, X.; Li, Z.; Pei, L.; Chen, G.; Liu, Z.; Chen, Y.; Liu, C.; Wang, M.; Zhang, M. Paleo-Tethyan Ocean Evolution and Indosinian Orgenesis in the East Kunlun Orogen, Northern Tibetan Plateau. *Minerals* **2022**, *12*, 1590. [CrossRef]